ARTICLES
https://doi.org/10.1038/s41591-022-01718-1

nature medicine

Check for updates

OPEN

Pancreatic islet cryopreservation by vitrification achieves high viability, function, recovery and clinical scalability for transplantation

Li Zhan[1,8], Joseph Sushil Rao[2,3,8], Nikhil Sethia[4], Michael Q. Slama[5], Zonghu Han[1], Diane Tobolt[2], Michael Etheridge[1], Quinn P. Peterson[5,6], Cari S. Dutcher[1,4], John C. Bischof[1,7,9] and Erik B. Finger[2,9] ✉

Pancreatic islet transplantation can cure diabetes but requires accessible, high-quality islets in sufficient quantities. Cryopreservation could solve islet supply chain challenges by enabling quality-controlled banking and pooling of donor islets. Unfortunately, cryopreservation has not succeeded in this objective, as it must simultaneously provide high recovery, viability, function and scalability. Here, we achieve this goal in mouse, porcine, human and human stem cell (SC)-derived beta cell (SC-beta) islets by comprehensive optimization of cryoprotectant agent (CPA) composition, CPA loading and unloading conditions and methods for vitrification and rewarming (VR). Post-VR islet viability, relative to control, was 90.5% for mouse, 92.1% for SC-beta, 87.2% for porcine and 87.4% for human islets, and it remained unchanged for at least 9 months of cryogenic storage. VR islets had normal macroscopic, microscopic, and ultrastructural morphology. Mitochondrial membrane potential and adenosine triphosphate (ATP) levels were slightly reduced, but all other measures of cellular respiration, including oxygen consumption rate (OCR) to produce ATP, were unchanged. VR islets had normal glucose-stimulated insulin secretion (GSIS) function in vitro and in vivo. Porcine and SC-beta islets made insulin in xenotransplant models, and mouse islets tested in a marginal mass syngeneic transplant model cured diabetes in 92% of recipients within 24–48 h after transplant. Excellent glycemic control was seen for 150 days. Finally, our approach processed 2,500 islets with >95% islets recovery at >89% post-thaw viability and can readily be scaled up for higher throughput. These results suggest that cryopreservation can now be used to supply needed islets for improved transplantation outcomes that cure diabetes.

Despite 100 years of therapeutic development since the discovery of insulin, current diabetes therapies, such as continuous glucose monitors, insulin pumps and closed-loop systems, remain a treatment for the condition rather than a cure of the disease[1]. Although recent decades have seen substantial progress in the development of islet transplantation as a potential cure for diabetes[2], one of the main limitations of this approach is that transplants from a single donor are often insufficient to achieve insulin independence in the recipient[3,4]. Frequently, two, three or more donor islet infusions totaling 700,000 to >1 M islet equivalents (IEQs) are required for a 'typical' 70-kg recipient[5,6], adding risks associated with repeat surgical interventions and multiple rounds of strong immunosuppression induction.

One strategy for overcoming the donor supply problem is to pool islets from multiple donors, achieving high islet dosage with a single infusion[7,8], increasing efficacy and reducing risk. Although several groups have shown the feasibility of culturing islets for extended periods (weeks to months)[9], the majority have reported reduced islet recovery and loss of endocrine function over time[10,11]. Thus, large clinical trials often limit culture to 48–72 h before transplant[12]. This inability to culture or store high-quality islets for more than a few days after isolation, however, makes islet pooling logistically impractical. A second strategy is to develop an alternative islet source, such as SC-derived islets, which offer the exciting promise of an unlimited islet supply[13,14] and decreased reliance on limited donor availability. SC-derived islets produce insulin in response to glucose, restore normoglycemia in some animal transplant models and have been tested in phase 1 and 2 trials in humans. However, heterogeneity in endocrine cell composition and variability in function[13] lead to considerable batch-to-batch variability[15], requiring extensive pretransplant validation of each lot, during which time SC-islets deteriorate in culture. The inability to store islets before use is a common challenge in both strategies. Longer-term storage is required to overcome the supply chain barriers limiting the availability of sufficient quantities of islets and to enable adequate quality assessment before transplant.

Cryopreservation, or the stabilization of biomaterials at an ultralow temperature (less than −150 °C), can achieve pooling, long-term banking, and off-the-shelf availability of viable cells and tissues[16,17]. Conventional cryopreservation techniques utilize slow cooling (i.e., <1 °C min^{-1}) of biological substances to a dehydrated frozen state with the presence of extracellular ice. The addition of a low concentration (~2 M) of CPAs helps stabilize cells during cryopreservation and improves cellular viability. Despite extensive

[1]Department of Mechanical Engineering, University of Minnesota, Minneapolis, MN, USA. [2]Department of Surgery, University of Minnesota, Minneapolis, MN, USA. [3]Schulze Diabetes Institute, University of Minnesota, Minneapolis, MN, USA. [4]Department of Chemical Engineering and Materials Science, University of Minnesota, Minneapolis, MN, USA. [5]Department of Physiology and Biomedical Engineering, Mayo Clinic, Rochester, MN, USA. [6]Center for Regenerative Medicine, Mayo Clinic, Rochester, MN, USA. [7]Department of Biomedical Engineering, University of Minnesota, Minneapolis, MN, USA. [8]These authors contributed equally: Li Zhan, Joseph Sushil Rao. [9]These authors jointly supervised this work: John C. Bischof, Erik B. Finger. ✉e-mail: efinger@umn.edu

investigation (Supplementary Table 1 and the studies reviewed in Kojayanet al.[18]), challenges persist for islet cryopreservation due to ice-related injury (i.e., suboptimal viability), inability to achieve clinical scalability and use of non-clinically accepted components (i.e., fetal bovine serum) required to improve viability.

A promising alternative to existing conventional cryopreservation methods is ice-free vitrification; that is, rapid cooling of a biomaterial to a glass-like state[19,20]. To avoid ice formation, the cooling and subsequent warming rates need to exceed the critical cooling rate (CCR) and critical warming rate (CWR), respectively. Increasing CPA concentration (>4 M) can lower the required CCR and CWR to attainable levels but cause toxicity in cells and tissues, especially at higher temperatures (>4 °C). Thus, there is a critical balance point that avoids both injury from ice and from CPA toxicity while maintaining clinical scalability. Previous islet vitrification strategies were limited to small volumes with low islet quantities (<150 islets in microliter volumes of CPA solution; Supplementary Table 1) to ensure sufficient cooling and warming rates, and volumetric scale-up reduced the cooling and warming rates and led to ice formation, compromising viability. To our knowledge, no published technique has simultaneously achieved islet cryopreservation with high viability, function and recovery in a clinically scalable protocol (Supplementary Table 1).

To achieve this goal, we conducted systematic investigations on the CPA (formulation, concentration, loading and unloading) and vitrification method (enhancing cooling and rewarming rates) to develop a new islet cryopreservation method that simultaneously achieves high recovery, viability, functionality and scalability. We validated our methods on mouse, porcine, human and human SC-derived islets. Extensive in vitro assessments of viability, metabolic health and insulin secretion were performed. Finally, using syngeneic and xenogeneic transplant models, we demonstrated that after VR, islets remain viable in vivo, produce insulin, respond to glycemic challenge and cure diabetes. The overview of our technique is summarized in Fig. 1a.

Results

Preparation of pancreatic islets. For this study, we tested cryopreservation and postwarming function of mouse, porcine, human and SC-beta islets. SC-beta islets were clusters generated by differentiation of a human embryonic SC line (HUES8) in six stages using nongenetic programming while in 3D suspension culture[21]. Supplementary Fig. 1 shows an example of SC-beta cell-specific characterization during each stage of differentiation. Mouse islets and SC-beta islets were used for initial development, and the approach was then validated using human and porcine islets.

Development of a scalable VR method. We first screened various VR approaches and assessed their performance in cooling, rewarming and scalability. We compared three commonly used droplet-based VR strategies: (1) copper dish cooling and convective warming, (2) copper dish cooling and laser nanowarming (gold nanorods were added to the droplet to generate heat upon laser irradiation) and (3) convective cooling and warming using a cryotop device (Supplementary Fig. 2; details in Methods). Briefly, 10–20 islets in a 2-µl droplet were vitrified and subsequently rewarmed. We assessed the cooling and warming rates by direct measurement or by estimation via modeling (Supplementary Table 2)[16]. Post-thaw viability was 56%, 62% and 55% using approaches 1, 2 and 3, respectively. Overall, each of these approaches suffered from suboptimal viability and potential challenges in scalability (details in Supplementary Results and Discussion).

To overcome these droplet-based limitations, we next tested a cryomesh system that can successfully cryopreserve *Drosophila melanogaster* embryos[22]. The cryomesh consists of a nylon mesh (38-µm pore size) attached to a plastic handle. After loading CPA in islets while in suspension, the islets were transferred to a cryomesh support, and excess CPA solution was removed by wicking; this is a critical step, as it reduces the bulk of the thermal mass in the system, leaving a thin layer of islets on the cryomesh surrounded by a minimal volume of CPA (Fig. 1b). By removing this excess fluid, the cooling and warming rates are increased by roughly an order of magnitude to 5.4×10^4 and 30.9×10^4 °C min^{-1}, respectively, during convective cooling/warming (Fig. 1c). CPA removal also increases the density of islets within the system versus a droplet. For instance, a tightly packed monolayer of islets on a 2 cm × 2 cm nylon mesh (i.e., 1.7×10^4 islets) is >95% of the volume on the cryomesh, whereas 20 islets in a 2-µl droplet occupy only 1.8% of the total volume. Supplementary Table 2 summarizes the performance of cryomesh, droplet and cryotop VR approaches, emphasizing both the improved cooling and warming rates and the ability to scale-up the cryomesh.

CPA loading and unloading protocol. Having established the thermal performance of the cryomesh system, we sought a CPA formulation and loading/unloading protocol that would avoid ice formation while minimizing toxicity. Through a correlation between CPA concentration and CWR (equation (S2)), we estimated that the minimal CPA concentration in the interior of an islet should be 42–44 wt% to avoid devitrification (ice formation) during rewarming at 30.9×10^4 °C min^{-1} using the cryomesh (Fig. 1d). CPA toxicity can occur from both chemical and osmotic injury. To avoid injury, we tested stepwise CPA addition to minimize osmotic damage (i.e., extreme volume shrinkage below 60% or volume swelling above 153%) during loading and unloading, also assessing chemical toxicity as a function of step durations and a variety of CPA formulations.

To develop an optimized loading and unloading CPA protocol, we first fabricated a microfluidic device to measure islet biophysical parameters, including osmotic inactive volume (V_b), membrane water permeability (L_p) and CPA permeability (ω). V_b was measured by recording the final equilibrium volume of islets in various concentrations of hypertonic NaCl solution (Fig. 2b, lower panel). The Boyle–van't Hoff plots indicate that the osmotically inactive volume for mouse and SC-beta islets were 0.5 and 0.4, respectively (Fig. 2c). The membrane permeability parameters (L_p, ω) were determined by recording the characteristic shrink–swell behavior of islets upon exposure to CPA solutions containing 15 wt% propylene glycol (PG), ethylene glycol (EG) and dimethyl sulfoxide (DMSO) at 4 °C and 21 °C (Supplementary Fig. 3). The 'shrink' occurs due to high water permeability upon initial CPA exposure, driving water efflux from the islets. This shrink is followed by a 'swell' as permeable CPA diffuses across the cell membrane and water slowly re-enters the islets (Fig. 2b, upper panel). We used the two-parameter model based on L_p and P_s ($=\omega RT$, R is gas constant, T is absolute temperature) to fit the experimental shrink-swell curves (details in Methods). As shown in Fig. 2e, the water (L_p) and CPA permeability (ω) have larger values at a higher temperature for both mouse and SC-beta islets. The different cellular compositions between mouse and SC-beta islets likely led to the difference in permeability values between the two islet types. Although the above describes the shrink–swell during loading, the inverse occurs during unloading, which is a swell followed by a shrink, as noted elsewhere[23].

With these parameters (V_b, L_p and ω), the intracellular CPA concentration, islet volume and chemical toxicity during a multistep loading and unloading were modeled (equations (2) and (3) in Methods, equation S1 in Supplementary Methods). After optimization, our CPA loading protocol used the following 10-min step intervals: 21 °C at 1.3 M, 4 °C at 3.2 M and 4 °C at 6.5 M (Fig. 2f; details in Supplementary Results and Discussion). The volume excursions of mouse and SC-beta islets remained within the osmotic tolerances (Fig. 2g). The model predicted CPA concentration to be 6.2 M inside mouse islets and 6 M for SC-beta islets (Fig. 2h).

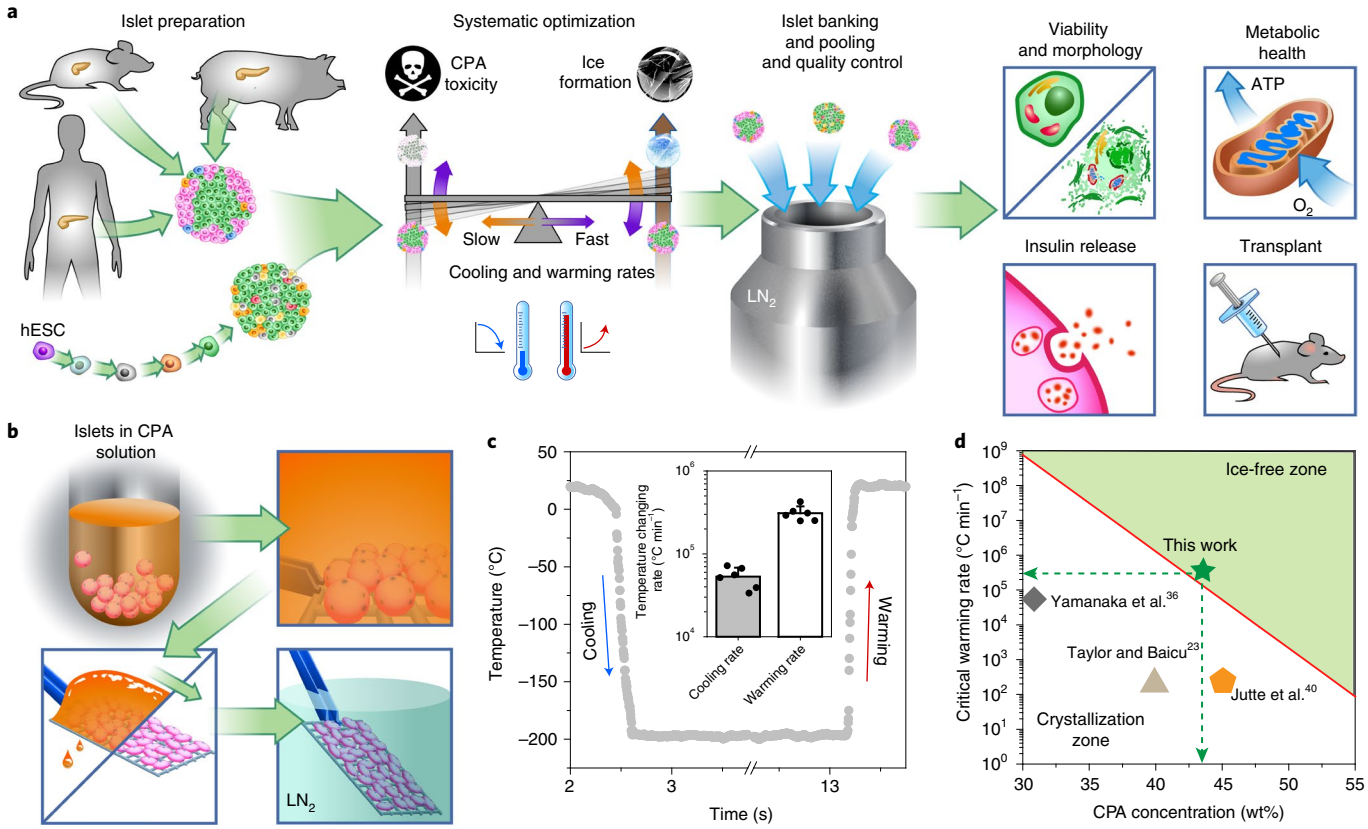

Fig. 1 | Overview of the study and the cooling/warming rates of cryomesh. a, Cryopreservation can be the cornerstone of an islet supply chain, allowing pooling, banking, and quality control before transplant. Model systems used to explore this include mouse, porcine and human islets and SC-beta islets. To achieve high recovery, viability, function and scalability simultaneously, systematic optimization of interrelated parameters, including CPA toxicity, ice formation and cooling and warming rates during VR cryopreservation, was performed in these islet systems. The achieved cooling and warming rates can adjust the balance between CPA toxicity and ice formation. Islet morphology, viability, metabolic health and in vitro and in vivo function were evaluated after VR cryopreservation. hESC, human embryonic stem cell. **b**, Schematic of cryomesh VR (not to scale). After CPA loading, islets in suspension were transferred to the cryomesh, and excessive CPA solution was removed before being plunged into liquid nitrogen (LN_2). **c**, Representative measured temperature profile of cryomesh VR. Inset is the achieved cooling and warming rates ($n=6$, data presented as mean ± s.d. with individual data points). **d**, Correlation of CWR and CPA concentration (equation (S2) in Supplementary Materials) indicates that ~44 wt% CPA is minimally required to avoid lethal ice using cryomesh VR and shows where other studies have failed to use a CPA with an adequate CWR to avoid ice under their thermal performance conditions.

CPA formulation optimization. To optimize the CPA formulation, we tested three overall CPA concentrations (33%, 44% and 54%) consisting of PG, EG, DMSO or mixtures. We used qualitative and quantitative live/dead staining to measure SC-beta islet viability for each CPA after loading and unloading (Fig. 2f) and again after VR. Qualitative measurements were determined by confocal imaging of intact islets after staining with acridine orange (AO) and propidium iodide (PI) (Fig. 3a). For quantitative measurement, islets treated with CPA with or without VR were dissociated to single cells and stained with AO/PI, and the percentage of live (AO^+/PI^-) cells was counted (Fig. 3b). Viability measured after loading and unloading reflected the toxicity of CPA. Further decrease in viability after VR presumably reflected ice-related injury during cooling and rewarming.

After CPA loading and unloading, EG demonstrated the least islet toxicity of the three individual components, followed by DMSO and PG (Fig. 3c). When mixtures were used at the same total concentration (44%), a mixture of EG and DMSO provided the least toxicity (cell viability was 96.4% of control), outperforming EG or DMSO alone. Islet viability also remained high (93.3% of control) after VR and remained essentially unchanged over 24 h of post-VR culture (Fig. 3d,e). Decreasing the mixture concentration (to 34%) led to lower post-VR viability due to ice formation; increasing the concentration (to 54%) resulted in lower viability due to CPA toxicity (Fig. 3c). The best-identified CPA formulation (22% EG + 22% DMSO) was used throughout the study.

Viability and morphology of VR islets. Using the optimized CPA formulation, loading and unloading conditions and cooling/rewarming cryomesh system, we examined islet morphology, viability, DNA fragmentation (TdT-mediated dUTP nick end labeling (TUNEL) stain) and Annexin V translocation following VR. We compared VR to healthy live control, dead control (ethanol-treated) and conventionally cryopreserved (i.e., slow cooling in 15% DMSO) islets (Fig. 4). Following VR, each of the four islet types (mouse, human, porcine and SC-beta) had an overall appearance and viability similar to fresh control islets and much better than conventionally cryopreserved islets (Fig. 4a). VR islets had smooth borders, rounded/oblong shape, and a normal histological appearance indistinguishable from fresh islets, whereas many conventionally cryopreserved islets demonstrated disruption of macroscopic architecture. The differences were even more evident on ultrastructural examination using transmission electron microscopy (TEM) (Fig. 4a, bottom). TEM imaging showed that the cell and nuclear

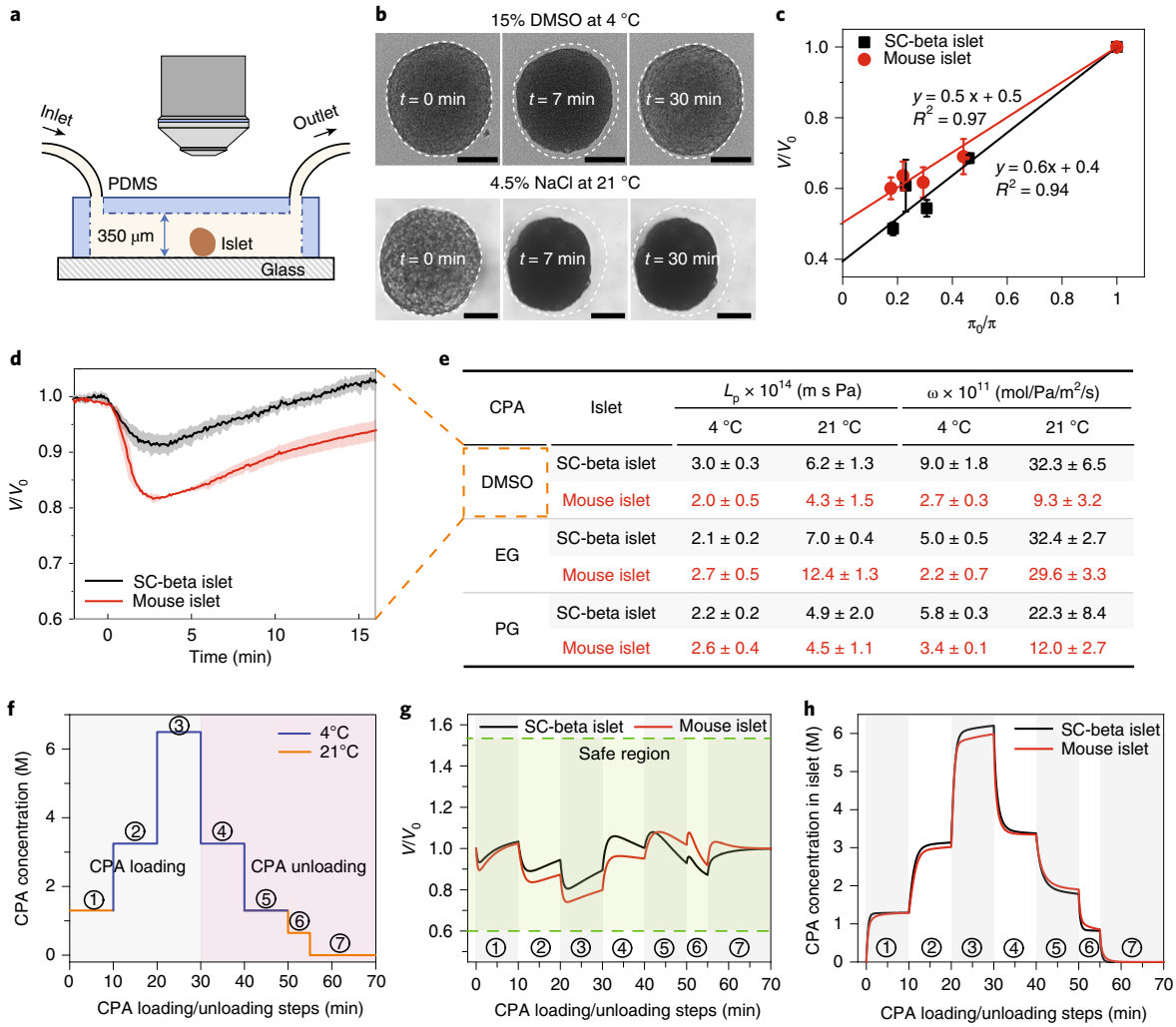

CPA	Islet	$L_p \times 10^{14}$ (m s Pa)		$\omega \times 10^{11}$ (mol/Pa/m^2/s)	
		4 °C	21 °C	4 °C	21 °C
DMSO	SC-beta islet	3.0 ± 0.3	6.2 ± 1.3	9.0 ± 1.8	32.3 ± 6.5
	Mouse islet	2.0 ± 0.5	4.3 ± 1.5	2.7 ± 0.3	9.3 ± 3.2
EG	SC-beta islet	2.1 ± 0.2	7.0 ± 0.4	5.0 ± 0.5	32.4 ± 2.7
	Mouse islet	2.7 ± 0.5	12.4 ± 1.3	2.2 ± 0.7	29.6 ± 3.3
PG	SC-beta islet	2.2 ± 0.2	4.9 ± 2.0	5.8 ± 0.3	22.3 ± 8.4
	Mouse islet	2.6 ± 0.4	4.5 ± 1.1	3.4 ± 0.1	12.0 ± 2.7

Fig. 2 | Islet biophysical property measurement and CPA loading/unloading protocol design. a, Schematic of the microfluidic device used to measure the biophysical properties of the islets (not to scale). The morphological changes of the islets were recorded via a microscope. PDMS, polydimethylsiloxane. **b**, Top: When subjected to 15 wt% DMSO at 4 °C, the islet first shrinks and then swells. Upon exposure to hypertonic CPA, water exits the cells, and the islet shrinks. CPA then diffuses across the cell membranes, followed by water re-entering the cell, leading to swelling back towards their initial state. Bottom: The islet remained shrunk in NaCl solution as the cells are impermeant to salt. Scale bars, 100 µm. **c**, Boyle–van't Hoff plots of mouse and SC-beta islets display the normalized islet volume (V/V_0) as a function of the osmolality ratio of isotonic and hypertonic NaCl solution (π_0/π). The osmotic inactive volume (V_b) that does not participate in the osmotic response can be estimated by extrapolating the linear fit to $\pi_0/\pi = 0$. Further details can be found in Methods ($n = 4$ for SC-beta islets, $n = 8$ for mouse islets). **d**, Normalized volume of mouse and SC-beta islets versus time demonstrating the shrink–swell behavior when exposed to 15 wt% DMSO at 21 °C ($n = 3$ for mouse islets, $n = 9$ for SC-beta islets). **e**, Summary table of mouse and SC-beta islets water (L_p) and CPA (ω) permeability at 4 °C and 21 °C ($n = 3$–9; the exact sample size can be found in Supplementary Fig. 3). The red color represents mouse islet in panels **c**,**d**,**g**,**h**, and is used in panel **e** to maintain consistency with the rest of the panels. **f**, Stepwise loading (steps 1–3) and unloading (steps 4–7) of 22 wt% EG + 22 wt% DMSO for islets. **g**, Modeled islet normalized volume change during CPA loading/unloading using the measured biophysical properties. The volume of both mouse and SC-beta islets remained in the safe region. **h**, Modeled CPA concentration in the mouse and SC-beta islets. For **c**–**e**, data are presented as mean ± s.d.

membranes, mitochondria, secretory granules and other organelles appeared intact in VR islets. In contrast, conventionally cryopreserved islets had gross qualitative changes in cell appearance, reduced numbers of mitochondria and secretory granules and substantial blebbing of cellular and nuclear membranes.

We next used AO/PI staining to measure changes in viability associated with each islet cryopreservation technique. Qualitatively, VR islets appeared similar to live control islets, with only a slight increase in the number of red (necrotic or dead) cells (Fig. 4c and Supplementary Fig. 5) for each of the four islet types. Conventionally cryopreserved islets showed much more cell death. Following cryopreservation, a separate set of islets was dissociated into a single-cell suspension and tested for viability on a per-cell basis (Fig. 4b). Post-VR viability, relative to control, was 90.5% for mouse, 92.1% for SC-beta, 87.2% for porcine and 87.4% for human. The viability was unchanged over 9 months of cryopreservation (88.3% for mouse islets and 91.8% for SC-beta). Conventional cryopreservation resulted in lower viability (59.1–62.2%) than VR islets.

Although we primarily examined overall islet cell viability, to evaluate the viability of insulin expressing (beta) cells specifically, we costained intact or dissociated islets with fixable live/dead dyes and anti-insulin antibodies and then assessed beta cell viability by confocal microscopy (qualitative measures, Supplementary Fig. 6) and FACS (quantitative measures, Supplementary Fig. 7) and found

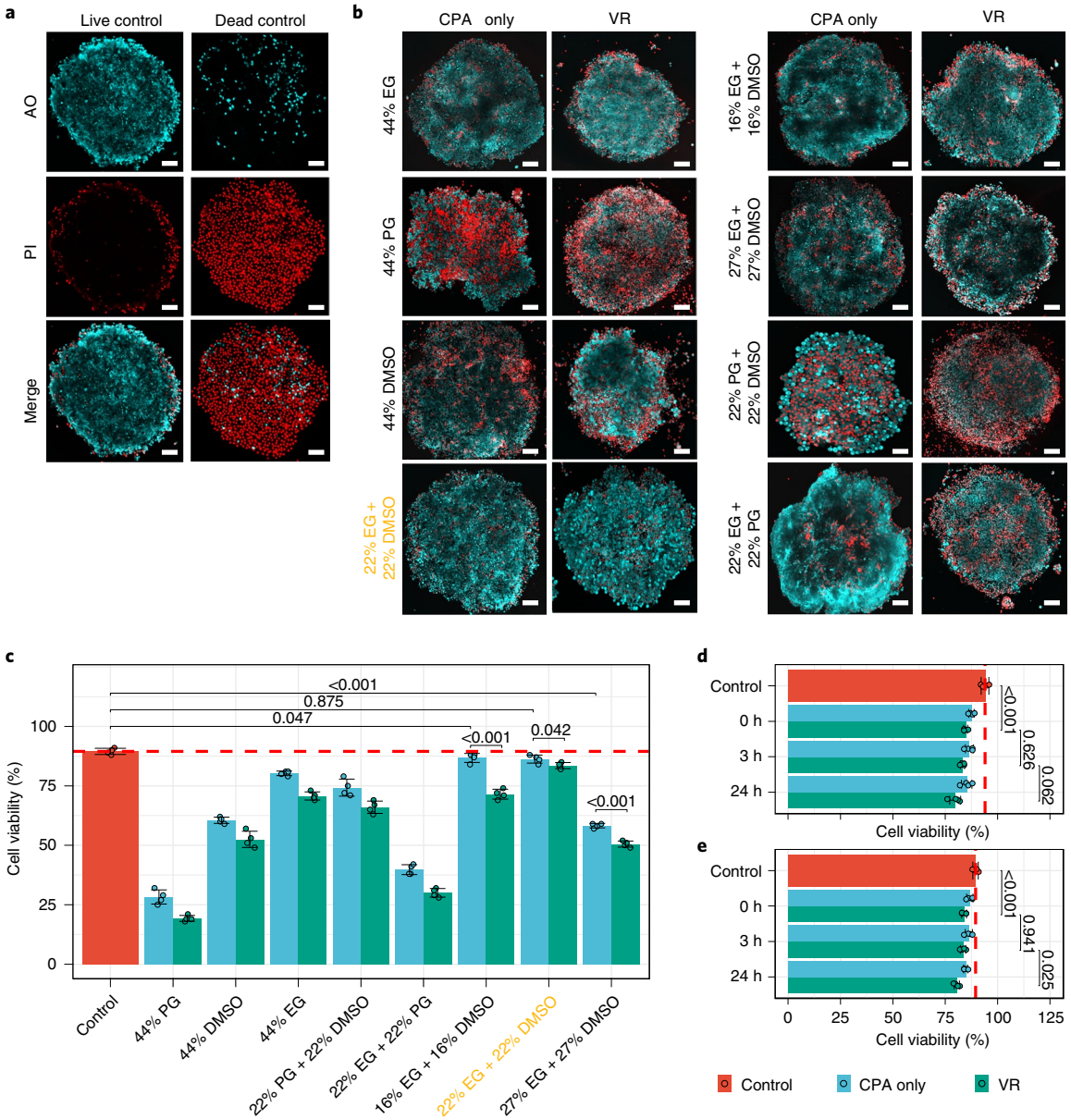

Fig. 3 | CPA formulation optimization for high post-VR viability. a, Confocal microscope images of live and dead controls of SC-beta islets stained with AO (cyan) and PI (red). **b**, Confocal microscope images (AO/PI merge) of CPA-treated (CPA loading and unloading only) and VR-treated (CPA loading, VR and CPA unloading) SC-beta islets. Various CPA formulations were examined. **c**, Cell viability of CPA-only-treated (cyan), VR-treated (green) and live control (red) SC-beta islets. Islets were dissociated into single cells, and viability was then measured. The yellow text in **b**,**c** is used to highlight the optimal condition. One-way analysis of variance (ANOVA) with Tukey post hoc test was used to compare groups, and *P* values from informative pairwise comparisons are shown ($n = 4$). **d**,**e**, For mouse (**d**) and SC-beta (**e**) islet cell viability after different culture time (0, 3 and 24 h) after CPA-only treatment and then after VR treatment. One-way ANOVA with Tukey post hoc test was used to compare groups, and informative pairwise comparisons are shown ($n = 4$). Scale bars, 100 µm. Data are shown as individual data points and mean ± s.d.

that both insulin positive and negative cells appeared to have similar viabilities (details in Supplementary Results and Discussion).

In addition to the observed low degree of cell death (PI^+ cells) with VR islets, we observed slightly more $TUNEL^+$ and cell-surface Annexin V^+ cells after VR in comparison to fresh control islets (Fig. 4d and Supplementary Fig. 8), suggesting both necrosis and apoptosis may contribute to the overall 8–12% decrease in viability with VR. Many more $TUNEL^+$ and Annexin V^+ cells were seen with conventionally cryopreserved islets. Compared with conventional cryopreservation, our VR technique resulted in substantial improvements in preserving the viability and morphology of the tested islet types.

Metabolic health of VR islets. Because viability measured by membrane permeability dyes represents a lagging indicator of islet dysfunction following treatment, we sought to examine other measures of islet health that could better define the expected islet function following cryopreservation. Specifically, metabolic health, particularly islet OCR, is predictive of islet function in vivo[24,25]. We first examined ATP levels in islets immediately post-VR and found that, at that time point, ATP content was notably lower than in control islets (Supplementary Fig. 9). However, ATP levels and other metabolic measures (OCR and mitochondrial membrane potential) were largely recovered after 3 h of culture. We used that time point for all further assessments.

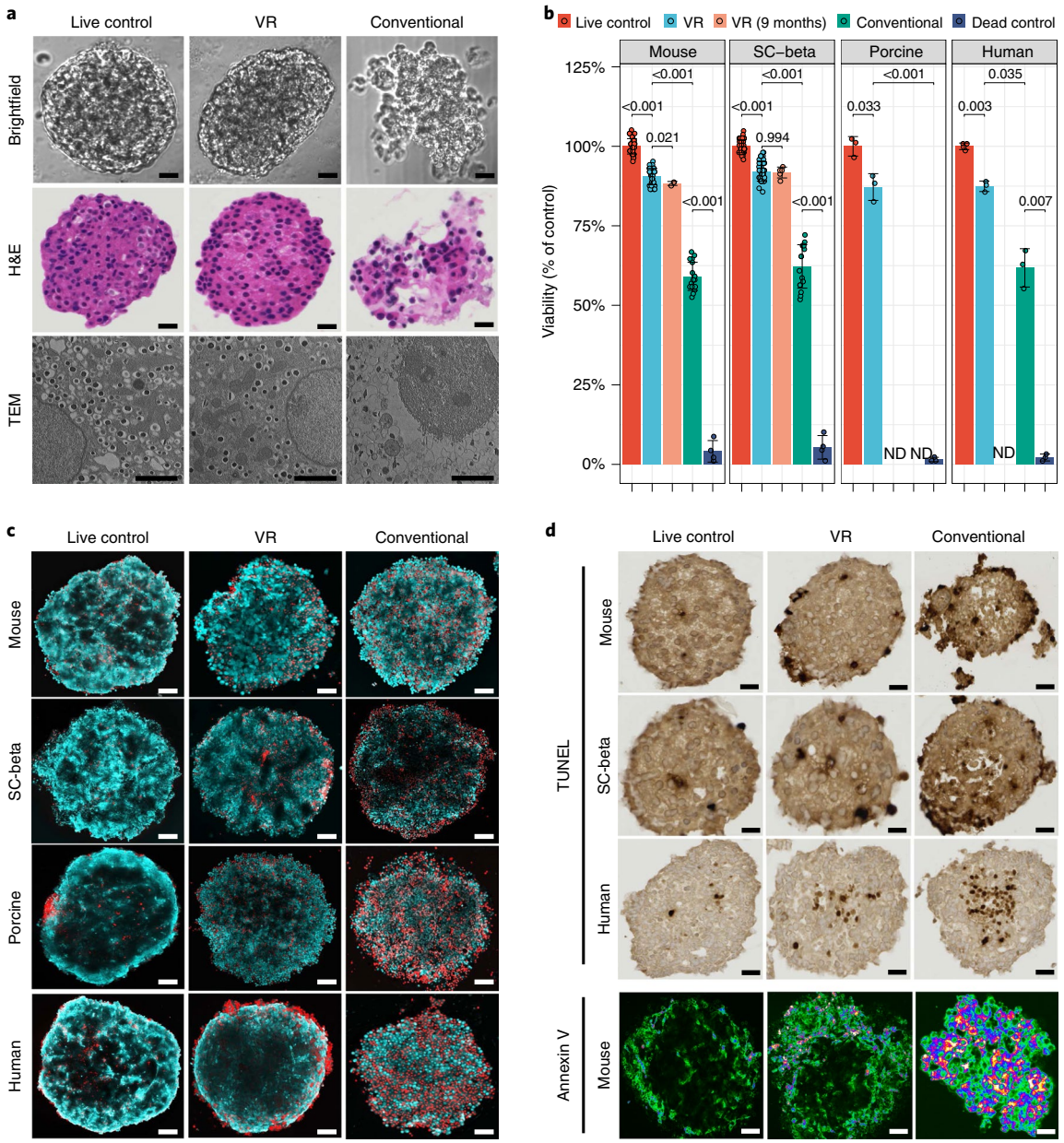

Fig. 4 | Viability and morphology of mouse, porcine, human and SC-beta islets following cryopreservation. a, Morphology of mouse islets from live control, VR (cryopreserved by VR) and conventional (cryopreserved by conventional slow freezing) was evaluated by brightfield microscopy, hematoxylin and eosin (H&E) histology, and TEM. For the conventional group, a mixture of intact and disrupted islets was observed. Examples of disrupted islet gross morphology due to ice formation are shown in the brightfield and H&E histology. **b**, Viability (percentage of live control) of mouse, SC-beta, porcine and human islets from treatment groups including live control, VR, VR 9 months (islets stored in LN_2 for 9 months before rewarming), conventional (cryopreserved by conventional slow freezing) and dead control (treated by 75% ethanol). ND, not done. One-way ANOVA with Games–Howell post hoc test was used to compare groups, and *P* values from informative pairwise comparisons are shown ($n = 3$–34 per group; exact number in Supplementary Table 3). **c**, Confocal microscope images (AO/PI) of mouse, SC-beta, porcine and human islets from treatment groups, including live control, VR and conventional. **d**, TUNEL-stained images of mouse, SC-beta and human islets from treatment groups, including live control, VR and conventional. Bottom panel is Annexin V staining of mouse islets from the same treatment groups. Scale bars represent 2 μm for TEM, 50 μm for brightfield images, 70 μm for histology and TUNEL images and 100 μm for all fluorescence images. Data are shown as individual data points and mean ± s.d.

Mitochondrial membrane potential in each of the four islet types was measured by tetramethylrhodamine ethyl ester (TMRE) staining and qualitative and quantitative confocal microscopy. The overall signal intensity was somewhat lower for VR islets than live control (65.7–86.3% of control), but when adjusted for viable cell content, TMRE intensity was 75.1–93.7% of control (Fig. 5b, left). The difference in TMRE intensity may be due to slower recovery in the center of the islets where there was some central lucency. This appearance appeared to improve further with 24 h of culture (Supplementary Fig. 9). TMRE staining intensity for conventionally cryopreserved islets was 37–42% of control islets (Fig. 5b).

The number and appearance of mitochondria seen by TEM of VR islets were qualitatively similar to control islet cells (Fig. 4a, bottom). Similar to the TMRE findings, overall ATP levels in

VR islets were slightly less than in the fresh control islets (Fig. 5b, right). These data suggest that cellular machinery to produce ATP remained intact, but ATP levels had not yet been fully restored to control values at the time point assayed.

Having shown intact mitochondria, we next looked at cellular respiration to assess whether VR islets were consuming oxygen to restore ATP. When compared to fresh control islets, VR islets showed a similar pattern of changes in OCR following stimulation with oligomycin (ATP synthase/complex V inhibitor), carbonyl cyanide 4-trifluorometheoxyphenylhydrazone (FCCP) (mitochondrial membrane uncoupling agent), and a mixture of rotenone (complex I inhibitor) and antimycin A (complex III inhibitor) (Fig. 5c). Conventionally cryopreserved islets showed a dampened OCR stress response. When comparing VR to fresh control in mouse, human and SC-beta islets, there were no differences in OCR for basal respiration, ATP production, proton leak, maximal respiration, spare respiratory capacity and nonmitochondrial respiration (Fig. 5d). These data suggest that VR islets maintain normal metabolic function as measured by cellular respiration.

In vitro insulin secretion by VR islets. We performed GSIS testing to determine if islets were functional in vitro. Mouse, SC-beta and human islets secreted insulin in response to glucose challenge and, for mouse and SC-beta, further with complete depolarization using KCl (Fig. 5e). Porcine islets were not tested. Human islets had maximal insulin release with high-glucose challenge but no further release with KCl. The stimulation indices (ratio of insulin released with exposure of high-glucose concentration to that of low glucose) for VR islets of each islet type measured were not different from control islets. Conventionally cryopreserved islets also showed insulin release in response to glucose challenge, but to a lesser degree. These data confirm that VR islets are viable, metabolically active and functional in vitro.

In vivo function of VR islets. As a final measure of post-VR islet function, we tested mouse, porcine and SC-beta islets in syngeneic and xenogeneic mouse transplant models (Fig. 6). Syngeneic mouse islets transplanted under the kidney capsule demonstrated function and restored normoglycemia within 48 h (Fig. 6a) and showed intense insulin immunofluorescence staining similar to control islets on posttransplant day 60, as did porcine and SC-beta xenotransplants in immunodeficient nonobese diabetic-*scid*-Il2rgc$^{-/-}$ (NSG) recipients (Fig. 6b). Mouse and porcine islets also had intense glucagon staining, although potentially with a slight qualitative reduction in signal intensity compared with control islets. As expected, SC-beta transplants showed weak glucagon staining, as these had been differentiated to a beta cell lineage[21,26]. Conventionally cryopreserved islets had very low insulin or glucagon staining intensity.

Using a xenogeneic transplant model, we next tested the function of SC-beta islets in vivo. SC-beta islets were transplanted in nondiabetic NSG mice, and random serum samples were obtained to measure human insulin at 4, 8 and 12 weeks posttransplant (Fig. 6d). VR islets secreted human insulin throughout the 12 weeks. Conventionally cryopreserved SC-beta islets had detectable human insulin production, but these levels were not statistically different from mock transplant recipients. At 14 weeks, the recipient mice were tested for fasting and stimulated human insulin production by intraperitoneal glucose injection (Fig. 6e). Conventionally cryopreserved islet transplant recipients did have detectable human insulin, but there was no increase in levels following stimulation. VR islet recipients had higher fasting levels than mock or conventionally cryopreserved islets and demonstrated a 2.3-fold increase following stimulation, confirming SC-beta function in vivo.

Fresh control, VR and conventionally cryopreserved mouse islets were next tested in a marginal mass (250 islets per recipient) syngeneic islet transplant model using streptozotocin-induced diabetic recipients. Overall, VR islets rapidly restored normoglycemia in 92% (11/12) of recipients within 24–48 h (Fig. 6a). In bivariate Kaplan Meier assessment, time to normoglycemia was not different from live control islet transplant recipients (log-rank test, $P=0.063$). One VR islet recipient demonstrated only partial function, potentially due to technical issues (i.e., islet leakage from kidney capsule). Blood sugar for that recipient fell below 200 mg dl^{-1} on posttransplant day 13 and then exhibited continued moderate hyperglycemia.

In contrast, conventionally cryopreserved islets failed to normalize blood glucose (BG) in all recipients, even with increased numbers of islets (450 islets per recipient). A subset of transplants underwent unilateral nephrectomy of the islet grafted kidney (Supplementary Fig. 10). Hyperglycemia developed rapidly in all mice, confirming that the transplanted islets, not the native recipient islets, controlled BG levels.

In the syngeneic transplants, glycemic control was extremely tight for VR islets. Random BG levels were not higher than those of control islet transplants throughout the posttransplant course (to 150 days posttransplant). To test the result of extended cryopreservation time, we vitrified islets, stored them in LN_2 for 9 months and then rewarmed them. These long-term stored islet transplants also demonstrated rapid BG normalization and glucose stability throughout the follow-up period.

To demonstrate the level of glycemic control, we performed intraperitoneal glucose tolerance testing (IPGTT) on posttransplant day 50 (Fig. 6c). There were no differences in the glucose response curves (Fig. 6c, left) or the areas under the curves (Fig. 6c, right) for untreated wild-type mice, fresh control islet transplants and VR transplants. Recipients of conventionally cryopreserved islets had a glycemic response similar to diabetic control mice.

Recovery and scalability. Islet recovery of our standard scale VR process (400–2,000 islets per test) was 96.8 ± 1.3% for mouse ($n=26$), 96.6 ± 1.7% for SC-beta ($n=26$), 91.3 ± 3.4% for porcine ($n=3$) and 96.7 ± 1.5% for human ($n=6$) islets (Supplementary Fig. 11). When we scaled up to medium throughput (2,500 islets per test), the recovery for mouse islets was 95.9 ± 1.2% (viability

Fig. 5 | Metabolic health and in vitro function of islets following cryopreservation. a, Mitochondrial membrane potential (via TMRE staining) of mouse, SC-beta, porcine and human islets from treatment groups, including live control, VR and conventional. **b**, Left: Quantification of TMRE staining intensity. Comparisons shown between live control and treatment groups were performed by Kruskal–Wallis and pairwise Wilcoxon tests ($n=3$–16 per group). Right: Measurement of ATP levels of four types of islets from live and dead control groups and cryopreservation groups (VR and conventional). One-way ANOVA with Games–Howell post hoc test was used to compare groups, and *P* values from informative pairwise comparisons are shown ($n=3$–12/group). **c**, Example OCR curve showing the change in OCR during Mito Stress testing in SC-beta islets and comparing live control, VR, conventional cryopreservation and dead control islets ($n=5$–8 per group at each time point). **d**, Compilation of the metabolic OCR parameters for each islet type and each treatment group. One-way ANOVA with Tukey post hoc test was used to compare groups, and significant ($P<0.05$) pairwise differences are shown ($n=3$–33 per group). **e**, In vitro GSIS assay for mouse, SC-beta and human islets from treatment groups, including live control, VR and conventional. One-way ANOVA with Tukey post hoc test was used to compare groups, and informative pairwise comparisons are shown ($n=3$–12/group). In **b**, **d** and **e**, relevant statistical comparison *P* values are included within the plots. Scale bars, 100 μm. Data are shown as individual data points and mean ± s.d. For **b**–**e**, the exact number of replicates can be found in Supplementary Table 3. RLU, relative light units.

of 89.4%, $n=3$), and SC-beta islet recovery was 98.2 ± 1.1% ($n=4$). Finally, in our initial proof-of-concept test of higher throughput SC-beta islet VR (10,000 islets per test), recovery was 92.6% ($n=1$).

Because the cryomesh system for VR is intrinsically unidimensional, scaling in the x and y dimensions is theoretically limited only by the container geometry. For these experiments, islets were vitrified on a 2 cm × 2 cm mesh at up to 4,250 islets per cm^2. To achieve

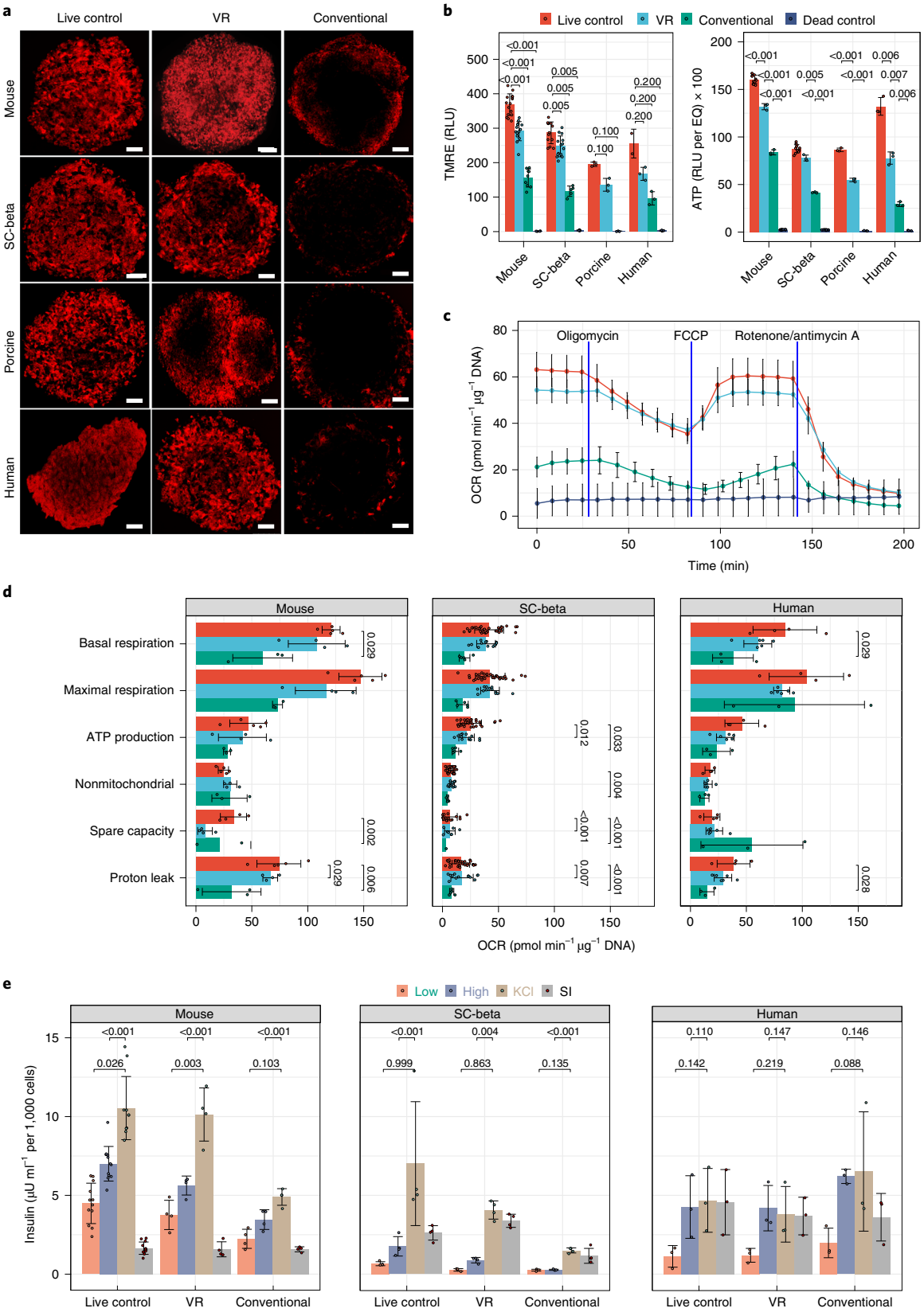

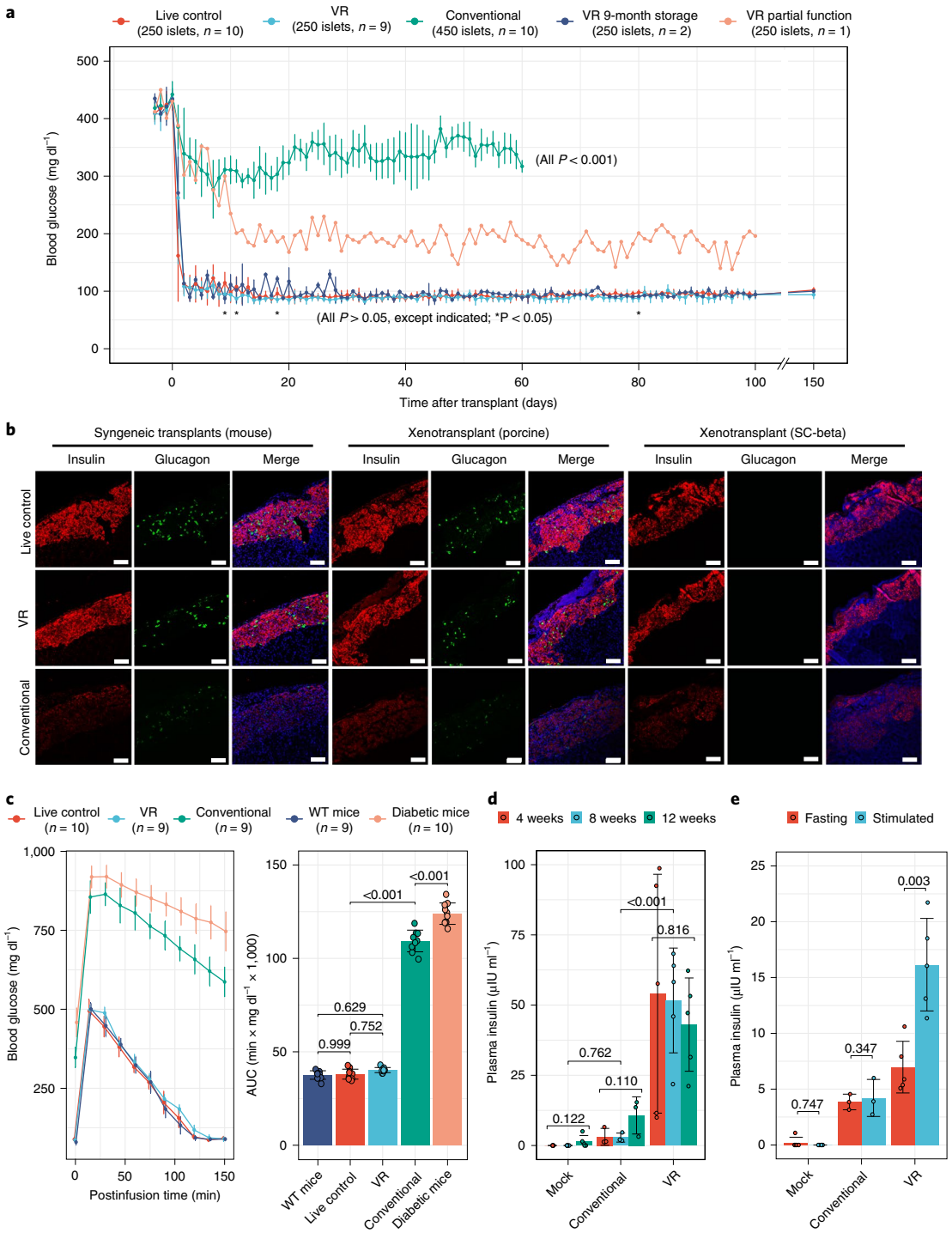

Fig. 6 | In vivo function of islets following cryopreservation. a, Blood glucose levels of streptozotocin-induced diabetic mice after syngeneic transplant of marginal mass mouse islets (250 islets per recipient) from treatment groups, including live control, VR, VR with 9-month cryopreserved storage (islets stored in LN_2 for 9 months) and conventional cryopreservation (450 islets per recipient). All pairwise comparisons with *P* value <0.05 are shown (*$P < 0.05$), as determined by one-way ANOVA with Games–Howell post hoc test [($n = 10$ (control and conventional cryopreservation), 9 (VR), 1 (VR partial function) and 3 (9-month storage and VR)). **b**, Insulin (red) and glucagon (green) staining in syngeneic (mouse) and xenogeneic (porcine and SC-beta) mouse transplant models. Treatment groups of islets include live control, VR and conventional. 4′,6-Diamidino-2-phenylindole staining (blue) is shown in the merged images. **c**, IPGTT of wild-type (WT) mice, diabetic mice and diabetic mice transplanted with live control, VR and conventional cryopreserved islets (left). Area under the curve (AUC) of IPGTT (right panel). Groups were compared by one-way ANOVA and Tukey post hoc test, and only informative pairwise comparisons are shown ($n = 9$–10 per group). **d**, Xenotransplant of SC-beta islets in NSG mice with nonfasting plasma human insulin levels at 4, 8 and 12 weeks after transplant. **e**, At 14 weeks, plasma insulin level of NSG mice after fasting and 30 min following stimulated insulin production by intraperitoneal glucose injection. For **d** and **e**, group comparison is by one-way ANOVA and Tukey post hoc test with informative comparisons shown ($n = 3$–5/treatment group). Scale bars, 200 μm. Data are shown as individual data points and mean ± s.d. For **c**–**e**, the exact number of replicates can be found in Supplementary Table 3.

clinically meaningful throughput, units of 100,000 islets could thus be preserved on 24-cm^2 cryomeshes.

Discussion

Transplantation of a sufficient number of high-quality, viable and functional pancreatic islets into a diabetic patient can cure this increasingly common and progressively debilitating disease. A major limitation affecting the success of islet transplantation is the lack of an on-demand supply of sufficient numbers of high-quality native or SC-derived islets, a limitation that is exacerbated by the inability to store these cellular products before use. Here, we show, for the first time, an effective method for long-term islet preservation that achieves high viability, recovery, function and scalability simultaneously. Such a method for pancreatic islet banking via cryopreservation could revolutionize the supply chain for islet isolation, allocation, and storage before transplant, increasing the overall utilization of deceased donor pancreases and curing more patients of diabetes.

Prior studies explored both the conventional methods (slow cooling) and vitrification (rapid cooling) for the cryopreservation of islets, achieving varying degrees of success (Supplementary Table 1). For example, Rajotte et al.[27,28] and other groups[29,30] demonstrated the conventional cryopreservation of islets using a standard CPA (2 M DMSO) but achieved only low to moderate viability and function and at limited throughput (10–100 islets). Improvements in the protocol (that is, different CPA) resulted in better function[31,32] or better throughput (≥10,000 islets)[33,34], but not both simultaneously. Conventional cryopreservation was tested in limited clinical trials[35] but was never fully adopted due partly to the use of fetal bovine serum, which comes with a risk of zoonotic infection. Meanwhile, several groups have tested vitrification (i.e., ice-free cryopreservation) as a favorable alternative to improve viability and function[23,36–39]. Initial studies demonstrated proof of principle, but with low islet throughput (50–300 islets) and partial function[23,40]. By changing the system's geometry through the use of droplets[41], hollow fibers[39] or mesh supports[37,38], other groups improved the cooling and heating rates and achieved modest improvements in function but at the cost of lower throughput (often just 25–100 islets at a time).

In addition to efficacy in cryopreserving freshly isolated mouse, porcine and human pancreatic islets, the VR approach was also effective for SC-derived human islets. SC-beta islets provide a promising source of human cells for beta cell replacement, demonstrating glucose-responsive insulin secretion in vitro and long-term glycemic control in diabetic mouse models[21,42]. Extensive efforts are underway to improve the SC-derived beta cell technology to achieve robust physiologic function; create efficient, low-cost differentiation methods; and improve the complement of endocrine cells (that is, produce with a mixture of alpha and beta cells)[43,44]. Nonetheless, a robust supply of high-quality SC-beta islets, such as enabled through cryopreservation, is still needed to realize off-the-shelf availability for future clinical adoption. Our cryopreservation method provides a potential solution, demonstrating high viability (92.1%) and in vitro and in vivo functionality of SC-beta islets, even after 9 months of storage in LN_2. Long-term storage would allow immune manipulation of prospective recipients, enable comprehensive islet quality control before transplantation and increase cost efficiency by allowing large batches to be cryopreserved in functional single-patient units. These results suggest that our new cryopreservation protocol may be a powerful means of improving the SC-beta islet supply chain, thereby increasing therapeutic options for diabetic patients.

For both SC-beta islets and deceased donor islets, the scalability of the cryopreservation method is essential. Further scale-up of our approach for a clinical meaningful throughput (i.e., ≥100,000 islets), can be achieved using larger cryomesh sizes and alternative form factors such as mesh stacking (Supplementary Fig. 12). For a larger cryomesh size, when the mesh is plunged rapidly and uniformly, the cooling and rewarming fluxes and thermal mass (per unit area) will remain independent of mesh size and shape, under the conditions that cooling/rewarming baths are sized adequately (i.e., larger than the cryomesh) and the rewarming bath is agitated. In addition, the remaining CPA solution (entrained due to surface tension) between the islets and cryomesh temporarily 'glues' the islets to the cryomesh, and islets do not detach from the cryomesh during storage in LN_2.

Our findings lay the groundwork for future clinical islet cryopreservation and suggest that high viability, functionality (in vitro and in vivo) and scalability can be achieved simultaneously during mouse, porcine, human and SC-beta islet cryopreservation. Further efforts are needed to address the limitations of our approach, including CPA optimization for human islets; further characterization of stress, adaptation and injury responses of islets; scale-up to a throughput of >300,000 islets per batch (typical yields for single-donor isolation are <300,000 IEQs[5]); and adaptation to clinical-grade processing (details in Supplementary Results and Discussion). We believe each of these limitations will be readily overcome in future development.

The implications of a successful method for islet cryopreservation before transplant are profound. Such technology has the following advantages: (1) improved efficacy through high-dose pooled donor islet transplants; (2) better opportunity for quality control and assessment; (3) better patient preparation by converting an unplanned operation into a planned event; (4) decreased risk by using a single islet infusion rather than repeated infusions; (5) improved opportunity for HLA matching of donor and recipient by selecting from a bank of available options rather than using the next donor in line; (6) facilitated tolerance induction protocols that require recipient preconditioning before transplants, such as tolerance achieved by apoptotic donor leukocytes infusion[45] or mixed chimerism with islets and donor-derived hematopoietic SC transplant; and (7) improved organ utilization by promoting islet isolation and banking from all appropriate donors rather than only 'optimal' donors that have been historically selected to maximize yields in hopes of single-donor transplants.

Online content

Any methods, additional references, Nature Research reporting summaries, source data, extended data, supplementary information, acknowledgements, peer review information; details of author contributions and competing interests; and statements of data and code availability are available at https://doi.org/10.1038/s41591-022-01718-1.

Received: 24 September 2021; Accepted: 26 January 2022;
Published online: 14 March 2022

References

1. Latres, E., Finan, D. A., Greenstein, J. L., Kowalski, A. & Kieffer, T. J. Navigating two roads to glucose normalization in diabetes: automated insulin delivery devices and cell therapy. *Cell Metab.* **29**, 545–563 (2019).
2. Shapiro, A. J. et al. Islet transplantation in seven patients with type 1 diabetes mellitus using a glucocorticoid-free immunosuppressive regimen. *N. Engl. J. Med.* **343**, 230–238 (2000).
3. Hering, B. J. et al. Phase 3 Trial of transplantation of human islets in type 1 diabetes complicated by severe hypoglycemia. *Diabetes Care* **39**, 1230–1240 (2016).
4. Vantyghem, M. C. et al. Ten-Year outcome of islet alone or islet after kidney transplantation in type 1 diabetes: a prospective parallel-arm cohort study. *Diabetes Care* **42**, 2042–2049 (2019).
5. Kaddis, J. S., Danobeitia, J. S., Niland, J. C., Stiller, T. & Fernandez, L. A. Multicenter analysis of novel and established variables associated with successful human islet isolation outcomes. *Am. J. Transplant.* **10**, 646–656 (2010).
6. Plesner, A. & Verchere, C. B. Advances and challenges in islet transplantation: islet procurement rates and lessons learned from suboptimal islet transplantation. *J. Transplant.* **2011**, 979527 (2011).
7. Scharp, D. W. et al. Results of our first nine intraportal islet allografts in type 1, insulin-dependent diabetic patients. *Transplantation* **51**, 76–85 (1991).

8. Warnock, G. L., Kneteman, N. M., Ryan, E. A., Rabinovitch, A. & Rajotte, R. V. Long-term follow-up after transplantation of insulin-producing pancreatic islets into patients with type 1 (insulin-dependent) diabetes mellitus. *Diabetologia* **35**, 89–95 (1992).
9. Gaber, A. O. & Fraga, D. Advances in long-term islet culture. *Cell Biochem. Biophys.* **40**, 49–54 (2004).
10. Schmied, B. M. et al. Transdifferentiation of human islet cells in a long-term culture. *Pancreas* **23**, 157–171 (2001).
11. Kin, T. et al. Risk factors for islet loss during culture prior to transplantation. *Transpl. Int.* **21**, 1029–1035 (2008).
12. Ricordi, C. et al. National Institutes of Health–sponsored Clinical Islet Transplantation Consortium phase 3 trial: manufacture of a complex cellular product at eight processing facilities. *Diabetes* **65**, 3418–3428 (2016).
13. Tremmel, D. M., Mitchell, S. A., Sackett, S. D. & Odorico, J. S. Mimicking nature-made beta cells: recent advances towards stem cell-derived islets. *Curr. Opin. Organ Transplant.* **24**, 574–581 (2019).
14. Pepper, A. R. et al. Posttransplant characterization of long-term functional hesc-derived pancreatic endoderm grafts. *Diabetes* **68**, 953–962 (2019).
15. Velazco-Cruz, L. et al. Acquisition of dynamic function in human stem cell-derived β cells. *Stem Cell Rep.* **12**, 351–365 (2019).
16. Khosla, K. et al. Characterization of laser gold nanowarming: a platform for millimeter-scale cryopreservation. *Langmuir* **35**, 7364–7375 (2019).
17. Zhan, L. et al. Conduction cooling and plasmonic heating dramatically increase droplet vitrification volumes for cell cryopreservation. *Adv. Sci.* **8**, 2004605 (2021).
18. Kojayan, G. G., Alexander, M., Imagawa, D. K. & Lakey, J. R. T. Systematic review of islet cryopreservation. *Islets* **10**, 40–49 (2018).
19. Khosla, K. et al. Cryopreservation and laser nanowarming of zebrafish embryos followed by hatching and spawning. *Adv. Biosyst.* **4**, 2000138 (2020).
20. Song, Y. C., Khirabadi, B. S., Lightfoot, F., Brockbank, K. G. & Taylor, M. J. Vitreous cryopreservation maintains the function of vascular grafts. *Nat. Biotechnol.* **18**, 296–299 (2000).
21. Pagliuca, F. W. et al. Generation of functional human pancreatic β cells in vitro. *Cell* **159**, 428–439 (2014).
22. Zhan, L., Li, M. G., Hays, T. & Bischof, J. Cryopreservation method for Drosophila melanogaster embryos. *Nat. Commun.* **12**, 2412 (2021).
23. Taylor, M. J. & Baicu, S. Review of vitreous islet cryopreservation: Some practical issues and their resolution. *Organogenesis* **5**, 155–166 (2009).
24. Papas, K. K. et al. Islet oxygen consumption rate (OCR) dose predicts insulin independence in clinical islet autotransplantation. *PLoS ONE* **10**, e0134428 (2015).
25. Papas, K. K. et al. Human islet oxygen consumption rate and DNA measurements predict diabetes reversal in nude mice. *Am. J. Transplant.* **7**, 707–713 (2007).
26. Veres, A. et al. Charting cellular identity during human in vitro β-cell differentiation. *Nature* **569**, 368–373 (2019).
27. Rajotte, R. V., Stewart, H. L., Voss, W. A. & Shnitka, T. K. Viability studies on frozen–thawed rat islets of Langerhans. *Cryobiology* **14**, 116–120 (1977).
28. Rajotte, R. V., Warnock, G. L. & Kneteman, N. N. Cryopreservation of insulin-producing tissue in rats and dogs. *World J. Surg.* **8**, 179–186 (1984).
29. Bank, H. L. & Reichard, L. Cryogenic preservation of isolated islets of Langerhans: two-step cooling. *Cryobiology* **18**, 489–496 (1981).
30. Nakagawara, G., Kojima, Y., Mizukami, T., Ono, S. & Miyazaki, I. Transplantation of cryopreserved pancreatic islets into the portal vein. *Transplant. Proc.* **13**, 1503–1507 (1981).
31. Miyamoto, M. et al. Development of a cryopreservation procedure employing a freezer bag for pancreatic islets using a newly developed cryoprotectant. *Cell Transplant.* **10**, 363–371 (2001).
32. Kojayan, G. et al. Improved cryopreservation yield of pancreatic islets using combination of lower dose permeable cryoprotective agents. *Cryobiology* **88**, 23–28 (2019).
33. Lakey, J. R., Warnock, G. L., Ao, Z. & Rajotte, R. V. Bulk cryopreservation of isolated islets of Langerhans. *Cell Transplant.* **5**, 395–404 (1996).
34. Miranda, P. M. et al. Human islet mass, morphology, and survival after cryopreservation using the Edmonton protocol. *Islets* **5**, 188–195 (2013).
35. Warnock, G. L. et al. Normoglycaemia after transplantation of freshly isolated and cryopreserved pancreatic islets in type 1 (insulin-dependent) diabetes mellitus. *Diabetologia* **34**, 55–58 (1991).
36. Yamanaka, T. et al. Direct comparison of Cryotop® vitrification and Bicell® freezing on recovery of functional rat pancreatic islets. *Cryobiology* **73**, 376–382 (2016).
37. Yamanaka, T., Goto, T., Hirabayashi, M. & Hochi, S. Nylon mesh device for vitrification of large quantities of rat pancreatic islets. *Biopreserv. Biobank* **15**, 457–462 (2017).
38. Nakayama-Iwatsuki, K. et al. Transplantation of rat pancreatic islets vitrified-warmed on the nylon mesh device and the silk fibroin sponge disc. *Islets* **12**, 145–155 (2020).
39. Nagaya, M. et al. An effective new cryopreservation procedure for pancreatic islets using hollow fiber vitrification. *Horm. Metab. Res.* **48**, 540–549 (2016).
40. Jutte, N. H., Heyse, P., Jansen, H. G., Bruining, G. J. & Zeilmaker, G. H. Vitrification of mouse islets of Langerhans: comparison with a more conventional freezing method. *Cryobiology* **24**, 292–302 (1987).
41. Sasamoto, H., Futami, M., Ando, Y. & Nakaji, S. Cryopreservation of rat islets of Langerhans by vitrification. *J. Artif. Organs* **15**, 283–289 (2012).
42. Vegas, A. J. et al. Long-term glycemic control using polymer-encapsulated human stem cell–derived beta cells in immune-competent mice. *Nat. Med.* **22**, 306–311 (2016).
43. Odorico, J. et al. Report of the key opinion leaders meeting on stem cell-derived beta cells. *Transplantation* **102**, 1223 (2018).
44. Peterson, Q. P. et al. A method for the generation of human stem cell-derived alpha cells. *Nat. Commun.* **11**, 2241 (2020).
45. Singh, A. et al. Long-term tolerance of islet allografts in nonhuman primates induced by apoptotic donor leukocytes. *Nat. Commun.* **10**, 3495 (2019).

Methods

Islet isolation methods. Institutional animal care and use committees from the University of Minnesota (protocol 1905-37028A) and the Mayo Clinic (protocol A00003973) approved the animal studies. Mice were housed with a 14-h on/10-h off light cycle, 68–74 °F ambient temperature and 30–70% humidity in specific pathogen-free (for NSG mice) or conventional (for C57BL/6 mice) facilities.

Mouse islets were isolated from C57BL/6 female retired breeders (age unspecified, Charles River Laboratories) by collagenase (CIzyme RI, VitaCyte) digestion and Histopaque (Millipore Sigma) density gradient enrichment[46]. Islets were then handpicked and cultured in a bioreactor (ABLE Biott reactor, BWV-S03A) in S3 media for 16 h before use. Human islets were purchased from a commercial vendor (Prodo Laboratories) and cultured in PIM(S) Complete media (Prodo Laboratories) for up to 7 days before use. Porcine islets were isolated from adult Landrace pigs[47].

SC-derived islet differentiation. HUES8 cells were cultured as spheroids in 500-ml spinner flasks (Corning, 3153)[21]. Suspension cultures were established by seeding 150 million cells (5×10^5 cells ml^{-1}) in mTeSR1 media (STEMCELL Technologies, 85850) with 10 µM Y27632 (R&D Systems, 1254) and maintained at 70 r.p.m. inside the humidified incubator at 37 °C, 5% CO_2 and 100% humidity. Media was changed at 48 h to mTeSR1 without Y27632. Cells were passaged every 72 h by dispersing to single cells using Accutase (Millipore Sigma, A6964) with mechanical disruption and resuspended in fresh mTeSR1 with Y27632.

SC-beta differentiations were initiated after 3 days of SC spheroid formation and expansion in mTeSR1 media inside a spinner flask[21,26]. Clusters were allowed to settle by gravity, and the media was replaced with protocol-specific media including appropriate growth factors. Cell differentiation was directed sequentially to definitive endoderm, primitive gut tube, pancreatic progenitor 1, pancreatic progenitor 2, endocrine progenitors and finally into SC-beta[26]. Basal media types (S1, S2, S3 and BE5) were supplemented with inductive signals (details in the Supplementary Methods). The SC-beta islets were characterized by flow cytometry (details in Supplementary Methods).

Measurement of islet biophysical parameters. The microfluidic devices used to measure islet biophysical parameters were fabricated using soft lithography procedures (details in Supplementary Methods). Handpicked islets were introduced into the device in retrograde fashion through the outlet hole. After initiating antegrade flow using islet media, CPA/salt solution of the desired concentration was loaded via a syringe pump. For CPAs, 15 wt% EG, PG and DMSO prepared in RPMI were used. For salt solutions, 1.8%, 2.7%, 3.6% and 4.5% sodium chloride prepared in deionized water were used. Once the islet settled on the channel floor, the CPA/salt solution flowrate was gradually increased while minimizing movement and rotation of the islet. The solution flow was stopped after at least five device volumes of solution had been pumped through the device. For experiments performed at 4 °C, the entire experiment was performed inside a cold room maintained at the same temperature. Islet cross-sectional area changes were recorded and analyzed using MATLAB to estimate islet spherical volume changes.

Fitting of L_p and ω. A two-parameter model using L_p (hydraulic conductivity, also called water permeability) and ω (CPA permeability) was applied to fit the experimental shrink–swell data[48]. The assumptions are detailed in Supplementary Materials. The osmotic inactive cell volume, V_b, was determined from the Boyle–van't Hoff relationship[49]. The Boyle–van't Hoff equation correlates the cell equilibrium volume with the osmolality of nonpermeating solution as below:

$$\frac{V}{V_0} = (1 - V_b)\frac{\pi_0}{\pi} + V_b, \tag{1}$$

where V is the cell equilibrium volume, V_0 is the isotonic cell volume, V_b is the osmotically inactive volume fraction of the cell, π_0 is the isotonic osmolality and π is the osmolality of the nonpermeating solution.

MATLAB was used to fit the L_p and ω of the mouse and SC-beta islets from the experimental shrink–swell curves. Modeling of islet volume change and intracellular CPA is based on the two-parameter 'uncoupled' model suggested by Kleinhans[48], as follows:

$$\frac{dV}{dt} = -L_p ART(C_S^e - C_S^i + C_C^e - C_C^i) \tag{2}$$

$$\frac{dn_c}{dt} = \omega RTA(C_C^e - C_C^i), \tag{3}$$

where V and A are the islet volume and surface area, respectively; n_C is the number of moles of CPA inside the islet; R is gas constant; T is the absolute temperature; L_p and ω are the hydraulic conductivity and membrane permeability to CPA, respectively; and C is the molality. The superscripts i and e denote intracellular and extracellular, respectively. The subscripts C and S denote permeating CPA and nonpermeating solutes, respectively.

Islet cryopreservation. *Conventional cryopreservation (slow cooling).* Islets were cryopreserved via a slightly modified slow freezing approach based on the previously established protocol by Rajotte et al.[50]. No fetal bovine serum or fetal calf serum was included in the CPA solution. At 21 °C, DMSO was added to the islet suspension to achieve a final concentration of 2 M in a cryovial. After a 25-min incubation with DMSO, the cryovial was placed in a −7.5 °C ethanol bath for 5 min. A metal rod was chilled in LN_2 and used to seed ice by touching the suspension in the cryovial. After 15 min of latent heat of fusion release, the cryovial was cooled at 0.25 °C min^{-1} to −40 °C using a control rate freezer (Kryo 560, Planer Limited) and then plunged into LN_2. Thawing was achieved using a 37 °C water bath. The thawed islets were placed in 0.75 M sucrose for 30 min at 0 °C to remove the intracellular CPA.

Cryomesh VR. The full-strength CPA used was 22 wt% EG + 22 wt% DMSO prepared in RPMI medium. To load the CPA, islets were first incubated in 20% CPA (i.e., 4.4 wt% EG + 4.4 wt% DMSO) for 10 min at 21 °C, followed by 50% CPA for 10 min at 4 °C and in 100% CPA for 10 min at 4 °C. The islet suspension was then transferred to the cryomesh placed on a wicking material (that is, paper towel). The CPA solution was wicked away through the nylon mesh and islets remained on the cryomesh. Clumping of islets was avoided. The cryomesh was quickly plunged into LN_2 and stored in a LN_2 tank. To thaw the islets, the cryomesh was plunged rapidly into the rewarming solution consisting of 11 wt% EG, 11 wt% DMSO and 5 wt% sucrose at 4 °C for CPA removal. After 10 min, the rewarming solution was diluted twofold using ice-cold 10 wt% sucrose solution, and the islets were incubated for another 10 min at 4 °C. The islets were then transferred to 21 °C, and the suspension was diluted twofold using 10 wt% sucrose solution. After 5 min, the islets were placed back in RPMI medium for 15 min as the last CPA removal step. At this time, all islets detached from the nylon mesh.

Cryotop VR. Using the same CPA loading procedure as in the cryomesh VR approach, 10–20 islets were included in a 2-µl droplet and placed on the cryotop. The cryotop was quickly plunged into LN_2 for vitrification. The rewarming and CPA removal process was the same as that performed in the cryomesh VR.

Copper dish cooling and convective warming. A 2 µl droplet, including 10–20 islets, was dropped onto a copper dish floating in LN_2 for vitrification. The vitrified droplet was convectively rewarmed in the unloading solution. The CPA removal steps were kept the same as in the cryomesh VR approach.

Copper dish cooling and laser nanowarming. Gold nanorods (nanoComposix) were added to the droplet to reach the concentration of 2.8×10^{10} parts ml^{-1}. After vitrifying the islet and gold nanorod embedded droplet (2 µl) on the prechilled copper dish, a 1064-nm pulse laser was used to rewarm the droplet[17]. The pulse length was 7.5 ms, and laser voltage was 250 V. A high-speed camera (Nac Image Technology, Q1v) was used to record the laser warming process at 4,000 frames per second.

TEM. The ultrastructures of islets were analyzed by TEM. Briefly, islets were fixed in 2.5% glutaraldehyde in 0.1 M sodium cacodylate buffer (pH 7.4) at 4 °C overnight and postfixed in 2% aqueous osmium tetroxide for 1 h, dehydrated in gradual ethanol (30% to 100%) and propylene oxide, embedded in Epon812 and cured for 48 h at 60 °C. Then, 65-nm ultrathin sections were collected onto 200-mesh copper grids and stained with uranyl acetate (15 min) and lead citrate (2 min) before examination by TEM. Images were captured with a FEI Tecnai G2 Spirit transmission electron microscope (Thermo Fisher Scientific).

Viability assessment. Qualitative measurement of intact islet viability was performed using AO and PI. Intact islets were stained with 8 ng ml^{-1} AO and 20 ng ml^{-1} PI (Millipore Sigma) for 2 min at room temperature, coverslipped and imaged using an Olympus Fluoview 3000 inverted confocal microscope (Olympus) with 502/525-nm filters for AO and 493/636-nm filters for PI. The images were captured at 4,020 × 4,020-pixel resolution using a 20× magnification objective. Note that the islet diameters in all of the confocal images, here and throughout the study, are increased due to coverslip compression used to increase effective imaging depth.

Quantitative viability was measured on dissociated islet cells. After islet treatment, islets were incubated in a dynamic culture flask at 70 r.p.m., 37 °C, and 5% CO_2 for 3 h in S3 media. The islets were dissociated into single-cell suspensions in TrypLE Express (Thermo Fisher Scientific, 12605010), quenched with S3 containing fetal bovine serum and stained with 8 ng ml^{-1} AO plus 20 ng ml^{-1} PI. After 15 s of incubation, 10 µl of the suspension was pipetted onto the Countess Cell Counting Chamber Slides (Thermo Fischer Scientific, C10228), and viability was quantified using a Countess II FL cell counter (Invitrogen by Thermo Fisher Scientific, AMQAF1000). The accuracy of the dissociated quantitative viability measurement technique was validated by comparing values to those obtained by image analysis of 3D reconstructions of confocal images of AO/PI-stained intact islets.

Mitochondrial membrane potential measurements. Before performing the assay, islet clusters received were incubated in a dynamic culture flask at 70 r.p.m., 37 °C and 5% CO_2. The islets were stained with 25 µl of 50 ng ml^{-1} reconstituted TMRE,

perchlorate (Biotium, 70005) at room temperature for 1 min and 45 s on microscope slides, coverslipped (Chase Scientific, ZA0294) and imaged using an Olympus Fluoview 3000 confocal inverted microscope (excitation/emission filters: 594/574 nm). The images were captured at 4,020 × 4,020 resolution using a 20× magnification objective. The membrane potential of the islet was quantified by measuring fluorescence intensity using Olympus CellSens Dimension software (v1.17).

ATP measurement. Islets were incubated in a dynamic culture flask at 70 r.p.m., 37 °C, and 5% CO_2 before each assay. Standard-sized islets (~150 µm) were handpicked, and three IEQs per well were placed in each well of black 96-well plates (Greiner Bio-One, 89131-680) in 50 µl RPMI at 37 °C. Then, 50 µl prewarmed Promega CellTiter-Glo 3D cell viability reagent was added to each well. ATP standard (Roche) was used as positive control and calibrate the results. The plate was sealed, covered with aluminum foil and placed on an orbital shaker at room temperature for 5 min at 80 r.p.m. The plate was then incubated at room temperature for 25 min without shaking. A BioTek Synergy 2 Multi-Mode Microplate Reader was used to capture the luminescence, which was analyzed using the BioTek Gen5 software and reported as relative light units per IEQ.

Cellular respiration/OCR measurement. Islets were incubated in a dynamic culture flask at 70 r.p.m., 37 °C and 5% CO_2 for 3 h before the assay was performed. Cellular respiration was measured using the Agilent Seahorse XF Mito Stress Test and Agilent SeaHorse xFe24 Islet Capture FluxPak (Agilent, 103418-100) plates and grids. Islets were handpicked into wells containing 500 µl culture media in sufficient numbers to cover 50% of the inner circle of each sample well. The islet capture screen was carefully and securely fit onto to the plate. Islets were washed twice with SeaHorse media (SeaHorse XF DMEM) (Agilent, 103575-100) supplemented with 1 mM pyruvate, 2 mM glutamine and 5.6 mM glucose and equilibrated for 1 h at 37 °C. Assay reagents were loaded in a previously hydrated sensor cartridge. The assay plate was inserted into a calibrated Agilent SeaHorse xFe24 analyzer, and the Mito Stress test was performed according to the manufacturer's protocol with the following optimized reagent concentrations: mouse islets (5 µM oligomycin, 1 µM FCCP and 10 µM each rotenone and antimycin A), SC-beta islets (10 µM oligomycin A, 2 µM FCCP and 10 µM each rotenone and antimycin A), human islets (50 µM oligomycin A, 10 µM FCCP and 10 µM each rotenone and antimycin A) and porcine islets (50 µM oligomycin A, 2.5 µM FCCP and 10 µM each rotenone and antimycin A). OCR values were obtained over 200 min. If the sampling rate differed between plates, the time course was scaled over the standard observation period.

For normalization between wells, the islets in each well were lysed in 1 M ammonium hydroxide + 0.2% Triton X-100. The DNA content was measured by PicoGreen assay (Molecular Probes) using standardized calibration controls for quantification on a BioTek Synergy 2 Multi-Mode Microplate Reader (BioTek). Individual cellular respiration parameters, including OCR for basal respiration, ATP production, proton leak, maximal respiration, spare respiratory capacity and nonmitochondrial respiration, were calculated and normalized to the DNA content obtained for individual wells.

TUNEL staining. Islet clusters received were incubated in a dynamic culture flask at 70 r.p.m., 37 °C and 5% CO_2 before the assay was performed. According to the manufacturer's protocol, apoptotic cells were stained using ApopTag Peroxidase in situ Apoptosis Detection Kit (Millipore Sigma, S7100). Following staining and washing, the slide was mounted by dehydrating with xylene, and a coverslip was applied using mounting media. The number of apoptotic cells in each islet was counted under a light microscope.

Annexin staining. Islet clusters received were incubated in a dynamic culture flask at 70 r.p.m., 37 °C and 5% CO_2 before the assay was performed. Then, 5× Annexin V binding buffer (Biotium, 99902) was diluted in deionized water to obtain 1× binding buffer. Islets were washed twice using 1× binding buffer. The staining solution was prepared by diluting Annexin V conjugate in 1× binding buffer to a final concentration of 2.5 µg ml^{-1} and incubated with the islets at room temperature for 15–30 min, protected from light. The islets were then washed with 1× binding buffer three times and imaged within 30 min using the Olympus Fluoview 3000 confocal inverted microscope with an excitation/emission of 490/515 nm under a 20× objective. The Ca^{2+} phospholipid-binding protein with a high affinity for phosphatidylserine was quantified by gating the false-color mapping fluorescence using Olympus CellSens Dimension software (v1.17) and statistically analyzed.

GSIS assay. GSIS assays were conducted to assess in vitro function of islets[26]. Briefly, islets were washed twice in low-glucose (3.3 mM glucose) Krebs Ringer buffer (KRB) (128 mM NaCl, 5 mM KCl, 2.7 mM $CaCl_2$, 1.2 mM $MgSO_4$, 1 mM Na_2HPO_4, 1.2 mM KH_2PO_4, 5 mM $NaHCO_3$, 10 mM HEPES and 0.1% FAF-BSA in deionized water). The islets were then loaded into 24-well transwell inserts (Millicell, cell culture insert, PIXP01250) and fasted in low-glucose KRB for 1 h at 37 °C. Islets were washed once in low-glucose KRB and then incubated in low-glucose KRB for 1 h at 37 °C. The volume of the KRB with low glucose, high glucose and KCl was 1 ml per well. After incubation, the supernatant was collected and stored at −20 °C until analysis. The islets were then transferred to high-glucose KRB (16.7 mM) for 1 h at 37 °C, and the supernatant was collected and stored. The islets were then transferred to low-glucose KRB with 30 mM KCl to observe depolarization conditions and incubated in this buffer for 1 h, and the supernatant was collected. Finally, the islets were dispersed via incubation with TrypLE and counted using a Countess automated cell counter (Thermo Fisher Scientific). Collected supernatants were analyzed by enzyme-linked immunosorbent assay for human insulin concentrations (ALPCO, 80-INSHUU-E01.1) and normalized for cell number. Mouse islet insulin was measured by HTRF (homogeneous time resolved fluorescence) assay (Cisbio PerkinElmer, 62IN1PEG).

Syngeneic mouse islet transplantation and IPGTT. C57BL/6 mice (6- to 8-week-old males, Charles River Laboratories) were rendered diabetic by single-dose (220 mg kg^{-1}) streptozotocin (Millipore Sigma, S0130) intraperitoneal injection. Blood glucose levels were measured after 4–7 days, and diabetes was confirmed by two successive daily measurements of >400 mg dl^{-1}. Marginal mass islet transplants of 250 islets per recipient[51] were performed under the recipient mouse's left kidney capsule. For all treatment groups, islets were randomly selected for transplantation, including islets of all sizes, both morphologically disrupted and intact islets. BG measurements were made daily. Transplant success was measured on the first day of two successive daily measurements of BG < 200 mg dl^{-1}. Graft failure was defined as the first day of two consecutive measurements >250 mg dl^{-1}.

On posttransplant day 50, IPGTT was performed by fasting mice for 16 h (overnight) and then injecting 2.5 g kg^{-1} glucose intraperitoneally and measuring BG every 15 min for 150 min.

To confirm that the transplanted islets were controlling BG levels and not a restoration of native beta cell function, left nephrectomy (including islet graft) was performed for a subset of transplants at posttransplant day 60, and return of hyperglycemia was verified. Day-60 explants were fixed and stained for insulin and glucagon.

Xenogeneic islet transplantation and IPGTT. SC-beta and porcine islets were transplanted under the kidney capsule of nondiabetic 6- to 12-week-old male (NSG) mice (Jackson Laboratory)[21]. Briefly, islet clusters containing a total of 5 × 10^6 cells were injected under the kidney capsule of male NSG mice. Control mice underwent a mock surgery in which saline was injected into the kidney capsule. Posttransplant facial bleeds were performed at weeks 4, 8 and 12 to measure human insulin levels. At 14 weeks posttransplant, modified IPGTT was performed. Mice were fasted for 16 h, and blood was collected before and 30 min after intraperitoneal injection of 2.5 g kg^{-1} glucose bolus. Serum was separated from blood using microvettes (Sarstedt, 20.1292.100), and human insulin was quantified using the human ultrasensitive insulin enzyme-linked immunosorbent assay (ALPCO, 80-INSHUU-E01.1). Following IPGTT, the graft-containing kidneys were explanted and stained for insulin and glucagon.

For porcine islet xenotransplants, 350 islets were transplanted under the kidney capsule of NSG mice (male or female, age 6–12 weeks). At 60 days posttransplant, the graft-containing kidneys were removed, fixed and stained for insulin and glucagon.

Insulin and glucagon immunofluorescence labeling. Recovered kidneys with transplanted islets under the kidney capsule were fixed in 70% alcoholic formalin (BBC Biochemical, 0460) and embedded in paraffin blocks. Then, 5-µm sections were cut using a microtome. The sections were deparaffinized using xylene and decreasing 100%, 90%, 80% and 70% EtOH concentrations. Slides were incubated with blocking buffer (5% bovine serum albumin (Millipore Sigma, B6917) in DPBS with Ca^{2+} and Mg^{2+} (Thermo Fisher Scientific, 14040141)) for 20 min and then stained with species-specific reagents as follows. For beta cell-specific viability experiments, intact mouse islets were stained with fixable live dead dye (Biotium, Live-or-Dye NucFix) before fixation, permeabilization and staining with anti-insulin antibodies (see below).

Syngeneic mouse islet transplants. Kidney sections were incubated at room temperature with FLEX polyclonal guinea pig anti-insulin antibody (Agilent, IR002) for 1 h at room temperature. The sections were gently washed five times using the blocking buffer and then incubated with recombinant rabbit anti-glucagon antibody (Abcam, ab92517) in blocking buffer (1:570) for 1 h. The sections were then washed five times gently with blocking buffer and incubated with goat anti-guinea pig immunoglobulin G (IgG) (H+L) secondary antibody (Alexa Fluor 488) (Abcam, ab150185; 1:250) and goat anti-rabbit IgG H&L (Alexa Fluor 647) (Abcam, ab150079) in blocking buffer (1:250) for 1 h at room temperature. After gently washing the sections with 4 °C DPBS with Ca^{2+} and Mg^{2+}, the sections were labeled with 4′,6-diamidino-2-phenylindole (Millipore Sigma, F6057), coverslipped (Chase Scientific, ZA0294) and placed at 4 °C for 2 h before imaging.

Porcine islet and SC-beta xenotransplants. Kidney sections were incubated at room temperature with mouse monoclonal anti-insulin antibody (K36aC10) (Abcam, ab6995) in blocking buffer (1:50 dilution) and recombinant rabbit anti-glucagon antibody (Abcam, ab92517) in blocking buffer (1:570) for 1 h at room temperature. The sections were then rinsed five times gently with blocking buffer and incubated

with goat anti-mouse IgG H&L (Alexa Fluor 647) (Abcam, ab150115) in blocking buffer (1:250) and goat anti-rabbit IgG H&L (Alexa Fluor 488) (Abcam, ab150077) in blocking buffer (1:300) for 1 h in room temperature. After gently washing the sections with 4 °C DPBS with Ca^{2+} and Mg^{2+}, the sections were labeled with 4′,6-diamidino-2-phenylindole (Millipore Sigma, F6057), coverslipped (Chase Scientific, ZA0294) and held at 4 °C for 2 h before imaging on an Olympus Fluoview 3000 inverted confocal microscope.

Statistics and reproducibility. Statistical analysis was performed in R version 4.0.3 (R Foundation for Statistical Computing). We included the exact number of independent experiments (n) and technical replicates for each relevant figure in Supplementary Table 3. Normality was tested with the Shapiro–Wilk test for continuous variables or graphically using qq plots and distribution histograms. Homogeneity of variance was assessed using Levene's test. For normal or near-normal group comparisons, ANOVA testing with pairwise post hoc Tukey HSD test was used to determine statistical differences. For groups with unequal variance, the Games–Howell test was used. Nonnormal variables were tested using the nonparametric Kruskal–Wallis test for overall significance and the pairwise Wilcox (Mann–Whitney U) test for individual group comparison. P values were adjusted for multiple comparisons. Time to event analysis was performed using the Kaplan–Meier method with the log-rank test of significance. Data are presented as mean ± s.d. unless specifically detailed otherwise. Full statistical treatment for each figure is presented in the Supplementary Data 2. Statistical testing was two sided, and a P value of <0.05 was considered significant.

Reporting Summary. Further information on research design is available in the Nature Research Reporting Summary linked to this article.

Data availability

All raw data have been archived for public access (https://doi.org/10.13020/yrva-zr31)[52].

Code availability

R version 4.0.3 was used for statistical analysis. MATLAB 2018b was used for calculating volume changes of islets from the experimentally recorded shrink–swell videos. MATLAB 2019a was used for the shrink–swell curve fitting and chemical toxicity cost–function evaluation. The custom codes are available upon request from the corresponding authors.

References

46. Melli, K. et al. Amplification of autoimmune response through induction of dendritic cell maturation in inflamed tissues. *J. Immunol.* **182**, 2590–2600 (2009).
47. Anazawa, T. et al. Improved method of porcine pancreas procurement with arterial flush and ductal injection enhances islet isolation outcome. *Transplant. Proc.* **42**, 2032–2035 (2010).
48. Kleinhans, F. W. Membrane permeability modeling: Kedem-Katchalsky vs a two-parameter formalism. *Cryobiology* **37**, 271–289 (1998).
49. de Freitas, R. C., Diller, K. R., Lakey, J. R. & Rajotte, R. V. Osmotic behavior and transport properties of human islets in a dimethyl sulfoxide solution. *Cryobiology* **35**, 230–239 (1997).
50. Cattral, M. S., Lakey, J. R., Warnock, G. L., Kneteman, N. M. & Rajotte, R. V. Effect of cryopreservation on the survival and function of murine islet isografts and allografts. *Cell Transplant.* **7**, 373–379 (1998).
51. Emamaullee, J. A. et al. The caspase selective inhibitor EP1013 augments human islet graft function and longevity in marginal mass islet transplantation in mice. *Diabetes* **57**, 1556–1566 (2008).
52. Bischof, John C; Finger, Erik B. Cryopreservation of Pancreatic Islets Experimental Data Repository 2022. Retrieved from the Data Repository for the University of Minnesota, https://doi.org/10.13020/yrva-zr31 (2022).

Acknowledgements

J.S.R. was supported by Schulze Diabetes Institute and Division of Transplantation at the Department of Surgery, University of Minnesota. The authors thank F. Zhou and W. Zhang from Characterization Facility of the University of Minnesota for help with TEM and C. Forster and A. Lewis of the University of Minnesota Clinical and Translational Science Institute for technical assistance with histology experiments. The authors acknowledge Schulze Diabetes Institute, Department of Surgery for use of their confocal microscope and for providing porcine islets. This work is supported by grants from Regenerative Medicine Minnesota (E.B.F. and J.C.B.), the National Science Foundation (EEC 1941543, J.C.B. and E.B.F.) and the National Institutes of Health (R01DK131209, J.C.B. and E.B.F.; R01DK117425, J.C.B. and E.B.F.; and R01HL135046, J.C.B. and E.B.F.). L.Z. acknowledges the Doctoral Dissertation Fellowship from the University of Minnesota, and J.C.B. acknowledges support from the Kuhrmeyer Chair in Mechanical Engineering and the Bakken Chair in the Institute for Engineering in Medicine from the University of Minnesota. P.P.Q. would like to thank the J.W Kieckhefer Foundation, the Stephen and Barbara Slaggie Family, and the Khalifa Bin Zayed Al Nahyan Foundation for supporting this work.

Author contributions

L.Z., J.S.R., J.C.B. and E.B.F. conceived and designed the study. L.Z., J.S.R., N.S., M.Q.S. and D.T. performed experiments and assembled the data. Z.H., N.S. and L.Z. performed modeling and assembled the data. C.S.D., Q.P.P., J.C.B. and E.B.F. coordinated and oversaw the study. J.C.B. and E.B.F. are the cosenior authors. All authors participated in discussion and interpretation of the data. L.Z., J.C.B. and E.B.F. wrote the manuscript with input from all authors.

Competing interests

L.Z., J.S.R., Z.H., N.S., M.E., C.S.D., J.C.B. and E.B.F. have filed a provisional patent application (serial no. 63/270,192) relevant to this study.

Additional information

Supplementary information The online version contains supplementary material available at https://doi.org/10.1038/s41591-022-01718-1.

Correspondence and requests for materials should be addressed to Erik B. Finger.

Peer review information *Nature Medicine* thanks Gordon Weir, Klearchos Papas and the other, anonymous, reviewer(s) for their contribution to the peer review of this work. Jerome Staal and Jennifer Sargent were the primary editors on this article and managed its editorial process and peer review in collaboration with the rest of the editorial team.

Reprints and permissions information is available at www.nature.com/reprints.

nature portfolio

Corresponding author(s): Erik Finger

Last updated by author(s): 1/18/2022

Reporting Summary

Nature Portfolio wishes to improve the reproducibility of the work that we publish. This form provides structure for consistency and transparency in reporting. For further information on Nature Portfolio policies, see our Editorial Policies and the Editorial Policy Checklist.

Statistics

For all statistical analyses, confirm that the following items are present in the figure legend, table legend, main text, or Methods section.

n/a	Confirmed
☐	☒ The exact sample size (*n*) for each experimental group/condition, given as a discrete number and unit of measurement
☐	☒ A statement on whether measurements were taken from distinct samples or whether the same sample was measured repeatedly
☐	☒ The statistical test(s) used AND whether they are one- or two-sided *Only common tests should be described solely by name; describe more complex techniques in the Methods section.*
☒	☐ A description of all covariates tested
☐	☒ A description of any assumptions or corrections, such as tests of normality and adjustment for multiple comparisons
☐	☒ A full description of the statistical parameters including central tendency (e.g. means) or other basic estimates (e.g. regression coefficient) AND variation (e.g. standard deviation) or associated estimates of uncertainty (e.g. confidence intervals)
☐	☒ For null hypothesis testing, the test statistic (e.g. *F*, *t*, *r*) with confidence intervals, effect sizes, degrees of freedom and *P* value noted *Give P values as exact values whenever suitable.*
☒	☐ For Bayesian analysis, information on the choice of priors and Markov chain Monte Carlo settings
☒	☐ For hierarchical and complex designs, identification of the appropriate level for tests and full reporting of outcomes
☒	☐ Estimates of effect sizes (e.g. Cohen's *d*, Pearson's *r*), indicating how they were calculated

Our web collection on statistics for biologists contains articles on many of the points above.

Software and code

Policy information about availability of computer code

Data collection	The following softwares were used for data collection: MATLAB 2018b, Olympus CellSens Dimension software (v1.17), BioTek Gen5, NXT v. 3.1 (ThermoFisher)
Data analysis	The following softwares were used for data analysis: R 4.0.3, MATLAB 2019a, Olympus CellSens Dimension software (v1.17), BioTek Gen5, and FlowJo v.10 (FlowJo, Ashland, OR)

For manuscripts utilizing custom algorithms or software that are central to the research but not yet described in published literature, software must be made available to editors and reviewers. We strongly encourage code deposition in a community repository (e.g. GitHub). See the Nature Portfolio guidelines for submitting code & software for further information.

Data

Policy information about availability of data

All manuscripts must include a data availability statement. This statement should provide the following information, where applicable:

- Accession codes, unique identifiers, or web links for publicly available datasets
- A description of any restrictions on data availability
- For clinical datasets or third party data, please ensure that the statement adheres to our policy

All data are deposited in the Data Repository of the University of Minnesota (DRUM) and are freely available.

Field-specific reporting

Please select the one below that is the best fit for your research. If you are not sure, read the appropriate sections before making your selection.

☒ Life sciences ☐ Behavioural & social sciences ☐ Ecological, evolutionary & environmental sciences

For a reference copy of the document with all sections, see nature.com/documents/nr-reporting-summary-flat.pdf

Life sciences study design

All studies must disclose on these points even when the disclosure is negative.

Sample size	Based on initial viability testing in mouse islets the normalized per cell viability was 100 ± 2.4% for control islets and 90.5 ± 2.6% for treated (vitrified and rewarmed). Using standard assumptions (alpha = 0.05, beta = 0.2, equal distribution between groups), we use the T statistic and determined the minimum sample size in each group (n = 3). However, since not all test parameters examined were normally distributed, we would need a group size of n ≥ 4 to be able to compare continuous variables with the possibility of demonstrating difference in the mean at a probability p < 0.05 for non-parametric tests. Thus, minimum sample size for statistical comparisons in this study were ≥ 3 for normally distributed parameters and ≥ 4 for non-normal.
Data exclusions	No data was excluded from the analysis
Replication	The number of replication in each experiment was represented by the number of data points in the presented figures. More than 3 replicates were performed in each experiment. All our attempts at replication were successful.
Randomization	Our sample were allocated randomly
Blinding	For different treatment groups, the islets were randomly selected and the outcome is determined by direct imaging and/or commercial readout devices. Wherever possible the outcome measures were determined by automated (i.e. computational) routine to minimize or avoid observational bias. Subjective observations (ie, gross appearance of islets) were clearly described as such in the text.

Reporting for specific materials, systems and methods

We require information from authors about some types of materials, experimental systems and methods used in many studies. Here, indicate whether each material, system or method listed is relevant to your study. If you are not sure if a list item applies to your research, read the appropriate section before selecting a response.

Materials & experimental systems

n/a	Involved in the study
☐	☒ Antibodies
☐	☒ Eukaryotic cell lines
☒	☐ Palaeontology and archaeology
☐	☒ Animals and other organisms
☒	☐ Human research participants
☒	☐ Clinical data
☒	☐ Dual use research of concern

Methods

n/a	Involved in the study
☒	☐ ChIP-seq
☐	☒ Flow cytometry
☒	☐ MRI-based neuroimaging

Antibodies

Antibodies used

FLEX Polyclonal Guinea Pig Anti-Insulin Antibody (Agilent; Cat # IR002)
Rabbit Anti-Glucagon antibody (abcam; Cat # ab92517)
Goat anti-Guinea Pig IgG (H+L) Secondary Antibody (Alexa® Flour 488) (abcam; Cat # ab150185)
Goat Anti-Rabbit IgG H&L (Alexa® Flour 647) (abcam; Cat # ab150079)
Mouse Monoclonal Anti-Insulin antibody [clone K36aC10] (abcam; Cat # ab6995)
Goat Anti-Mouse IgG H&L (Alexa Flour® 647) (Abcam; Cat # ab150115)
Goat Anti-Rabbit IgG H&L (Alexa® Flour 488) (abcam; Cat # ab150077)
goat anti-PDX1 (R&D Systems, AF2419)
mouse anti-NKX6.1 (DSHB, F55A12),
rabbit anti-chromogranin (Abcam, ab15160)
rat anti- c-peptide (DSHB, GN-ID4)
mouse anti-glucagon (Sigma, G2654).
donkey anti-goat Alexa Fluor 488 (Invitrogen, A-11055, 1:1,000)
donkey anti-rabbit Alexa Fluor 488 (Invitrogen, A-21206, 1:1,000)
donkey anti-rat Alexa Fluor 488 (Invitrogen, A-21208, 1:1,000)
donkey-anti-mouse-Alexa Fluor 647 (A-31571, 1:1,000)

Validation

FLEX Polyclonal Guinea Pig Anti-Insulin Antibody (Agilent; Cat # IR002)
Validation: "The antibody cross-reacts with insulin from several mammalian species. Specificity as determined by radioimmunoassay was 100% for human insulin, 100% for porcine insulin and less than 0.05% for glucagon and human growth hormone. This product has been optimized for use on human tissues."

Rabbit Anti-Glucagon antibody (abcam; Cat # ab92517)
Validation: IHC-P: Murine, human, and rat pancreatic tissue. IHC-Fr: Mouse pancreas tissue. WB: Capan-1 cell lysate, Mouse and rat pancreas tissue lysate
Publications (of 43 listed):
• Zhou L et al. Induced regulatory T cells suppress Tc1 cells through TGF-ß signaling to ameliorate STZ-induced type 1 diabetes mellitus. Cell Mol Immunol 18:698-710 (2021).PubMed: 33446887
• Wang MY et al. Glucagon blockade restores functional ß-cell mass in type 1 diabetic mice and enhances function of human islets. Proc Natl Acad Sci U S A 118:N/A (2021).PubMed: 33619103
• Kim GS et al. Optimal allogeneic islet dose for transplantation in insulin-dependent diabetic Macaca fascicularis monkeys. Sci Rep 11:8617 (2021).PubMed: 33883656
• Mimouni NEH et al. Polycystic ovary syndrome is transmitted via a transgenerational epigenetic process. Cell Metab 33:513-530.e8 (2021).PubMed: 33539777
• Yang X et al. Coregulator Sin3a Promotes Postnatal Murine ß-Cell Fitness by Regulating Genes in Ca2+ Homeostasis, Cell Survival, Vesicle Biosynthesis, Glucose Metabolism, and Stress Response. Diabetes 69:1219-1231 (2020).

Goat anti-Guinea Pig IgG (H+L) Secondary Antibody (Alexa® Flour 488) (abcam; Cat # ab150185)
Validation (example): "ICC/IF image of ab7291 stained HeLa cells. The cells were 100% methanol fixed (5 min) and then incubated in 1%BSA / 0.3M glycine in 0.1% PBS-Tween for 1h to permeabilise the cells and block non-specific protein-protein interactions. The cells were then incubated with the antibody (ab7291, 1µg/ml) overnight at +4°C. The cells were then incubated with ab7075, rabbit anti-mouse HRP conjugated antibody, for 1h at a 1/250 dilution. The cells were then incubated with ab34580, guinea pig anti-HRP antibody, for 1h at a 1/250 dilution. Lastly, the secondary antibody (green) was ab150185, polyclonal Secondary Antibody to Guinea pig IgG - H&L (Alexa Fluor® 488), used at 1µg/ml for 1h, as a quaternary antibody. DAPI was used to stain the cell nuclei (blue) at a concentration of 1.43µM."

References (of 25 listed):
• Almacellas E et al. Lysosomal degradation ensures accurate chromosomal segregation to prevent chromosomal instability. Autophagy 17:796-813 (2021).PubMed: 32573315
• Turecek J & Regehr WG Cerebellar and vestibular nuclear synapses in the inferior olive have distinct release kinetics and neurotransmitters. Elife 9:N/A (2020).PubMed: 33259288
• Matsunari H et al. Compensation of Disabled Organogeneses in Genetically Modified Pig Fetuses by Blastocyst Complementation. Stem Cell Reports 14:21-33 (2020).PubMed: 31883918
• Kurashige T et al. Hormonal Regulation of Autophagy in Thyroid PCCL3 Cells and the Thyroids of Male Mice. J Endocr Soc 4:bvaa054 (2020).PubMed: 32671315
• Zhou Y et al. RILP Restricts Insulin Secretion Through Mediating Lysosomal Degradation of Proinsulin. Diabetes 69:67-82 (2020).

Goat Anti-Rabbit IgG H&L (Alexa® Flour 647) (abcam; Cat # ab150079)
Validation: "ICC/IF image of ab6046 in HeLa cells. The cells were 100% methanol fixed (5 min), permeabilized with 0.1% Triton X-100 for 5 minutes and then incubated in 1%BSA / 10% normal goat serum / 0.3M glycine in 0.1% PBS-Tween for 1h to block non-specific protein-protein interactions. The cells were then incubated with the antibody (ab6046, 2µg/ml) overnight at +4°C. The secondary antibody ab150079 (shown in red) was used at 1µg/ml for 1h. DAPI was used to stain the cell nuclei (blue) at a concentration of 1.43µM. The negative control (inset) is a secondary-only assay to demonstrate low non-specific binding of the secondary antibody."
"Cross-reactivity of the polyclonal secondary antibody ab182016 was tested using a sandwich ELISA approach. The wells were coated with the indicated IgG standards at 1 µg/ml (50 µl/well) and incubated overnight at 4°C, followed by a 5% BSA blocking step for 2h at RT. ab182016 was then added starting at 1 µg/ml and gradually diluted 1/4 (50 µl/well), followed by incubation for 2h. For the detection Donkey anti-Goat IgG H&L (HRP) (ab6885) was used at 1/10,000 dilution (50 µl/well), followed by incubation for 1h at RT."
"Cross-reactivity of Goat anti-Rabbit IgG H&L (ab182016) and Goat anti-Rabbit IgG H&L obtained from two different vendors was tested using a sandwich ELISA approach. The wells were coated with the indicated IgG standards (Rabbit, Human, Mouse and Rat) at 1 µg/ml (50 µl/well) and incubated overnight at 4°C, followed by a 5% BSA blocking step for 2h at RT. Secondary antibodies were then added starting at 1 µg/ml and gradually diluted 1/4 (50 µl/well), followed by incubation for 2h. For the detection Donkey anti-Goat IgG H&L (HRP) (ab6885) was used at 1/10,000 dilution (50 µl/well), followed by incubation for 1h at RT."

References (of 176 listed):
• Wu F et al. Bleomycin A5 suppresses Drp1-mediated mitochondrial fission and induces apoptosis in human nasal polyp-derived fibroblasts. Int J Mol Med 47:346-360 (2021).PubMed: 33236140
• Daly AC et al. 3D bioprinting of high cell-density heterogeneous tissue models through spheroid fusion within self-healing hydrogels. Nat Commun 12:753 (2021).PubMed: 33531489
• Qian F et al. MiR-378a-3p as a putative biomarker for hepatocellular carcinoma diagnosis and prognosis: Computational screening with experimental validation. Clin Transl Med 11:e307 (2021).PubMed: 33634974
• Toro CA et al. The Human ApoE4 Variant Reduces Functional Recovery and Neuronal Sprouting After Incomplete Spinal Cord Injury in Male Mice. Front Cell Neurosci 15:626192 (2021).PubMed: 33679326
• Yao LC et al. Four potential microRNAs affect the progression of pancreatic ductal adenocarcinoma by targeting MET via the PI3K/AKT signaling pathway. Oncol Lett 21:326 (2021).

Mouse Monoclonal Anti-Insulin antibody [K36aC10] (abcam; Cat # ab6995)
Validation: "The antibody exhibits cross-reactivity with human proinsulin. This antibody recognizes purified insulin from the pancreas of human, bovine, horse, sheep, and proinsulin from human. Cross reaction has been observed with insulin containing cells in fixed sections of pancreas from human, porcine, dog, rabbit, bovine, sheep, rat, guinea pig and cat."
References (of 58 listed):

• Graham GV et al. Effects of long-acting analogues of lamprey GLP-1 and paddlefish glucagon on alpha- to beta-cell transdifferentiation in an insulin-deficient transgenic mouse model. J Pept Sci 27:e3328 (2021).PubMed: 33843129
• Kim GS et al. Optimal allogeneic islet dose for transplantation in insulin-dependent diabetic Macaca fascicularis monkeys. Sci Rep 11:8617 (2021).PubMed: 33883656
• Lafferty RA et al. Positive Effects of NPY1 Receptor Activation on Islet Structure Are Driven by Pancreatic Alpha- and Beta-Cell Transdifferentiation in Diabetic Mice. Front Endocrinol (Lausanne) 12:633625 (2021).PubMed: 33716983
• Moroki T et al. Databases for technical aspects of immunohistochemistry: 2021 update. J Toxicol Pathol 34:161-180 (2021).PubMed: 33976473
• Weng Q et al. STAT3 dictates ß-cell apoptosis by modulating PTEN in streptozocin-induced hyperglycemia. Cell Death Differ 27:130-145 (2020).

Goat Anti-Mouse IgG H&L (Alexa Flour® 647) (Abcam; Cat # ab150115)
Validation: "Specificity: ab150115 is specific to Mouse IgG. ab150115 has less than 47% cross-reactivity with rat IgG. Tested applications: Suitable for: IHC-Fr, ICC/IF, ELISA, IHC-P, Flow Cytometry"

References (from 197 listed):
• Lee SG et al. ?-Tocotrienol-Loaded Liposomes for Radioprotection from Hematopoietic Side Effects Caused by Radiotherapeutic Drugs. J Nucl Med 62:584-590 (2021).PubMed: 32826318
• Li Y et al. Songorine promotes cardiac mitochondrial biogenesis via Nrf2 induction during sepsis. Redox Biol 38:101771 (2021).PubMed: 33189984
• Li C et al. Changes in the expression of endothelial monocyte-activating polypeptide II in the rat hippocampus following status epilepticus. Int J Mol Med 47:699-707 (2021).PubMed: 33416103
• Zou W et al. ASK1/p38-mediated NLRP3 inflammasome signaling pathway contributes to aberrant retinal angiogenesis in diabetic retinopathy. Int J Mol Med 47:732-740 (2021).PubMed: 33416127
• Yang G & Zhao Y MicroRNA-490-3p inhibits inflammatory responses in LPS-induced acute lung injury of neonatal rats by suppressing the IRAK1/TRAF6 pathway. Exp Ther Med 21:152 (2021).

Goat Anti-Rabbit IgG H&L (Alexa® Flour 488) (abcam; Cat # ab150077)
Validation (example): "ICC/IF image of beta Tubulin staining in HeLa cells. The cells were 100% methanol fixed (5 min), permeabilized with 0.1% Triton X-100 for 5 minutes and then incubated in 1%BSA / 10% normal goat serum / 0.3M glycine in 0.1% PBS-Tween for 1h to block non-specific protein-protein interactions. The cells were then incubated with the primary antibody (ab6046, 5µg/ml) overnight at +4°C. The secondary antibody (green) was ab150077 Alexa Fluor® 488 goat anti-rabbit IgG (H+L) used at 2µg/ml for 1h. DAPI was used to stain the cell nuclei (blue) at a concentration of 1.43µM. The negative control (inset) is a secondary-only assay to demonstrate low non-specific binding of the secondary antibody."

References (from 1255 listed):
• Xiao M et al. Long non-coding RNA H19 promotes the proliferation, migration and invasion while inhibits apoptosis of hypertrophic scarring fibroblasts by targeting miR-3187-3p/GAB1 axis. Burns 47:654-664 (2021).PubMed: 32888745
• Gan L et al. Mesenchymal stem cells promote chemoresistance by activating autophagy in intrahepatic cholangiocarcinoma. Oncol Rep 45:107-118 (2021).PubMed: 33155663
• Li Y et al. Songorine promotes cardiac mitochondrial biogenesis via Nrf2 induction during sepsis. Redox Biol 38:101771 (2021).PubMed: 33189984
• Wei H et al. miR-34c-5p targets Notch1 and suppresses the metastasis and invasion of cervical cancer. Mol Med Rep 23:N/A (2021).PubMed: 33300051
• Niu YT et al. In the presence of TGF-ß1, Asperosaponin VI promotes human mesenchymal stem cell differentiation into nucleus pulposus like- cells. BMC Complement Med Ther 21:32 (2021).

goat anti-PDX1 (R&D Systems, AF2419)
Validation: "Detects human PDX 1/IPF1 in direct ELISAs and Western blots. In direct ELISAs, approximately 45% cross-reactivity with recombinant mouse PDX-1 is observed."

References (from 25 listed):
• Single-Cell Transcriptome Profiling Reveals &beta Cell Maturation in Stem Cell-Derived Islets after Transplantation. P Augsornwor, KG Maxwell, L Velazco-Cr, JR Millman. Cell Rep, 2020;32(8):108067.
• FGF2 Inhibits Early Pancreatic Lineage Specification during Differentiation of Human Embryonic Stem Cells. Authors: R Dettmer, K Cirksena, J Münchhoff, J Kresse, U Diekmann, I Niwolik, FFR Buettner, O Naujok. Cells, 2020;9(9).
• Targeting the cytoskeleton to direct pancreatic differentiation of human pluripotent stem cells. NJ Hogrebe, P Augsornwor, KG Maxwell, L Velazco-Cr, JR Millman. Nat. Biotechnol., 2020.
• HIV-1-induced cytokines deplete homeostatic innate lymphoid cells and expand TCF7-dependent memory NK cells. Y Wang, L Lifshitz, K Gellatly, CL Vinton, K Busman-Sah, S McCauley, P Vangala, K Kim, A Derr, S Jaiswal, A Kucukural, P McDonel, PW Hunt, T Greenough, J Houghton, M Somsouk, JD Estes, JM Brenchley, M Garber, SG Deeks, J Luban. Nat. Immunol., 2020;21(3):274-286.

mouse anti-NKX6.1 (DSHB, F55A12),
Validation: "Positive Tested Species Reactivity: Bovine, Human, Mouse, Porcine, Rat"

References (of 13 listed):
• Immunohistochemistry of pancreatic development in cattle and pig. Hyttel P. Anatomia, histologia, embryologia 39.2 (2010 Apr): 107-19.
• PCP effector proteins inturned and fuzzy play nonredundant roles in the patterning but not convergent extension of mammalian neural tube. Liu A. Developmental dynamics : an official publication of the American Association of Anatomists 240.8 (2011 Aug): 1938-48.

• Long-term persistence and development of induced pancreatic beta cells generated by lineage conversion of acinar cells. Zhou Q. Nature biotechnology 32.12 (2014 Dec): 1223-30.
• Matched miRNA and mRNA signatures from an hESC-based in vitro model of pancreatic differentiation reveal novel regulatory interactions. Laurent LC

rabbit anti-chromogranin (Abcam, ab15160)
Validation:: Validated in western blotting
References (of 173 listed):
• Yagishita Y et al. Constitutive Activation of Nrf2 in Mice Expands Enterogenesis in Small Intestine Through Negative Regulation of Math1. Cell Mol Gastroenterol Hepatol 11:503-524 (2021).PubMed: 32896624
• Chen Q et al. Paneth cell-derived growth factors support tumorigenesis in the small intestine. Life Sci Alliance 4:N/A (2021).PubMed: 33372038
• Jones BC et al. Paediatric gastric organoids as a tool for disease modelling and clinical translation. Pediatr Surg Int 37:317-324 (2021).PubMed: 33495862
• Quintero M et al. Cdk5rap3 is essential for intestinal Paneth cell development and maintenance. Cell Death Dis 12:131 (2021).PubMed: 33504792
• Yamazaki D et al. Role of adenomatous polyposis coli in proliferation and differentiation of colon epithelial cells in organoid culture. Sci Rep 11:3980 (2021).

rat anti- c-peptide (DSHB, GN-ID4)
Validation: " This antibody recognizes the C-peptide (aa 33-63 of proinsulin) which separates insulin B chain (aa 1-30) from insulin A chain (aa 66-86) in the proinsulin protein (minus signal peptide sequence). Stains C-peptide in mature granules and proinsulin in immature granules of islet beta-cells. The antibody does not cross-react with rodent C-peptide/proinsulin."

Referenes (from 15 listed):
• Tissue-specific expression of transfected human insulin genes in pluripotent clonal rat insulinoma lines induced during passage in vivo. Steiner DF. Proceedings of the National Academy of Sciences of the United States of America 85.18 (1988 Sep): 6652-6.
• Proinsulin-specific monoclonal antibodies. Immunocytochemical application as beta-cell markers and as probes for conversion. Madsen OD. Diabetes 36.10 (1987 Oct): 1203-11.
• Polyclonal origin of pancreatic islets in aggregation mouse chimaeras. Jami J. Development (Cambridge, England) 112.4 (1991 Aug): 1115-21.
• Ocular angiostrongyliasis in Semarang, Central Java. Margono SS. The American journal of tropical medicine and hygiene 26.1 (1977 Jan): 72-4.
• Efficient induction of pancreatic alpha cells from human induced pluripotent stem cells by controlling the timing for BMP antagonism and activation of retinoic acid signaling. Okochi H. PloS one 16.1 (2021): e0245204.

mouse anti-glucagon (Sigma, G2654).
Validation: "Specificity: Monoclonal Anti-Glucagon reacts with pancreatic glucagon in RIA and immunocytochemistry. The affinity constant of 6.1 x 10(8) L/M in RIA. The antibody weakly cross-reacts with gut glucagon (enteroglucagon) in an immunohistological assay. Cross-reactivity has been observed with glucagon-containing cells in fixed sections of pancreas from human, porcine, dog, rabbit, mouse, rat, guinea pig, and cat. The antibody reacts specifically against pancreatic glucagon and exhibits only very weak cross-reaction with gut glucagon (enteroglucagon). May be used for the immunohistochemical staining of Bouin's-fixed, and formalin-fixed, paraffin-embedded pancreatic tissue sections. Binds to glucagon with an affinity constant of 6.1 × 108 M-1 in RIA. Monoclonal anti-Glucagon antibody can be used as an analytical tool for quantification of the hormone. It can also be used for immunocytochemical staining of formalin fixed and Bouin-fixed, paraffin-embedded pancreatic tissue sections. Mouse anti-Glucagon antibody reacts specifically with pancreatic glucagon. The product has also shown cross reactivity with glucagon-containing cells in fixed sections of pancreas from dog, mouse, rat, rabbit, porcine, guinea pig, cat and human and weak cross reactivity for gut glucagon (enteroglucagon)."

References (selected):
• Glucagonoma syndrome: a review and update on treatment. John A M and Schwartz R A. Journal of the European Academy of Dermatology and Venereology : JEADV, 30(12), 2016-2022 (2016)
• Islet specific Wnt activation in human type II diabetes. Lee S H, et al. Experimental Diabetes Research, 2008 (2009)
• Isolation and purification of rat islet cells by flow cytometry. Akbarzadeh A, et al. Indian Journal of Clinical Biochemistry : IJCB, 23(1), 57-57 (2008)
• The metabolic actions of glucagon revisited. Habegger K M, et al. Nature reviews. Endocrinology, 6(1), 689-689 (2010)
• The Human Glucagon Gene Is Located on Chromosome 2. Tricoli J V, et al. Diabetes, 33(2), 200-202 (1984)

donkey anti-goat Alexa Fluor 488 (Invitrogen, A-11055, 1:1,000)
Validation: "Goat IgG (H+L) Cross-Adsorbed Secondary Antibody (A-11055) in Flow
Ishikawa cells (human endometrial adenocarcinoma cell line) were cultured according to standard protocol. The culture medium was aspirated and cells rinsed with Ca and Mg free HBSS. Cells were treated with 0.25% Trypsin and incubated at 37° for 5 minutes. Cells were aspirated and pelleted at 900 x g for 5 minutes. Cells were washed twice with PBS. The cells were then fixed with 4% paraformaldehyde in PBS for 15 minutes at room temperature. The cells were then washed as stated previously. Permeabilization and blocking was performed by incubating in 5% BSA and 0.1% Triton-X in PBS for 20 minutes at room temperature. The cells were then washed as previously stated. The primary antibody for OXTR (Product # PA5-19038) was used at a 1:200 dilution in a 5% BSA, PBS solution and incubated for 120 minutes at room temperature. The cells were washed as stated previously. The secondary Alexa 488 antibody (Product # A-11055) was used at a 1:2000 dilution in 5% BSA, PBS and incubated in the dark for 45 minutes. The cells were washed and resuspended in PBS and analyzed through flow cytometry. Data courtesy of the Antibody Data Exchange Program."
References (out of >200):
• Frontiers in neuroscience. "Induction of NTPDase1/CD39 by Reactive Microglia and Macrophages Is Associated With the Functional State During EAE." Jakovljevic M,Lavrnja I,Bozic I,Milosevic A,Bjelobaba I,Savic D,Sévigny J,Pekovic S,Nedeljkovic N,Laketa D. 2020

• Nature communications. " DDX5 plays essential transcriptional and post-transcriptional roles in the maintenance and function of spermatogonia." Legrand JMD,Chan AL,La HM,Rossello FJ,Änkö ML,Fuller-Pace FV,Hobbs RM. 2019.

• Journal of neuroinflammation. "Mesenchymal stem cells alleviate the early brain injury of subarachnoid hemorrhage partly by suppression of Notch1-dependent neuroinflammation: involvement of Botch." Liu W,Li R,Yin J,Guo S,Chen Y,Fan H,Li G,Li Z,Li X,Zhang X,He X,Duan C. 2019.

donkey anti-rabbit Alexa Fluor 488 (Invitrogen, A-21206, 1:1,000)

Validation: "Rabbit IgG (H+L) Highly Cross-Adsorbed Secondary Antibody (A-21206) in IHC
Immunofluorescence analysis of DA neurons using anti-tyrosine hydroxylase (TH) antibody. H9 ESCs were differentiated with PSC Dopaminergic neuron differentiation kit. H9 ESCs were specified to become midbrain floor plate (FP) progenitors which were further expanded and cryopreserved. Recovered FP progenitors were then matured for additional 14 days. Expression of TH was labeled with 1st antibody, anti-TH (Product # P21962) followed by 2nd antibody AlexaFluor488 donkey anti-rabbit (Product # A-21206, green). Nuclear DNA was stained with DAPI (blue)."

References (out of 543 references):
• Frontiers in neuroscience. "Induction of NTPDase1/CD39 by Reactive Microglia and Macrophages Is Associated With the Functional State During EAE." Jakovljevic M,Lavrnja I,Bozic I,Milosevic A,Bjelobaba I,Savic D,Sévigny J,Pekovic S,Nedeljkovic N,Laketa D. 2020

• The Journal of clinical investigation. Lkb1 deletion in periosteal mesenchymal progenitors induces osteogenic tumors through mTORC1 activation. Han Y,Feng H,Sun J,Liang X,Wang Z,Xing W,Dai Q,Yang Y,Han A,Wei Z,Bi Q,Ji H,Kang T,Zou W. 2019

• Cell communication and signaling. "bFGF-mediated pluripotency maintenance in human induced pluripotent stem cells is associated with NRAS-MAPK signaling." Haghighi F,Dahlmann J,Nakhaei-Rad S,Lang A,Kutschka I,Zenker M,Kensah G,Piekorz RP,Ahmadian MR. 2018

donkey anti-rat Alexa Fluor 488 (Invitrogen, A-21208, 1:1,000)
Validation: "Rat IgG (H+L) Highly Cross-Adsorbed Secondary Antibody (A-21208) in ICC/IF
Immunofluorescence analysis of Donkey anti-Rat IgG (H+L) Secondary Antibody, Alexa Fluor 488 conjugate was performed using A549 cells stained with alpha Tubulin (YL1/2) Rat Monoclonal Antibody (Product # MA1-80017). The cells were fixed with 4% paraformaldehyde for 10 minutes, permeabilized with 0.1% Triton™ X-100 for 10 minutes, blocked with 1% BSA for 1 hour and labeled with 2µg/mL Rat primary antibody for 3 hours at room temperature. Donkey anti-Rat IgG (H+L) Secondary Antibody, Alexa Fluor 488 conjugate (Product # A-21208) was used at a concentration of 1µg/mL in phosphate buffered saline containing 0.2 % BSA for 45 minutes at room temperature, for detection of alpha Tubulin in the cytoplasm (Panel a: green). Nuclei (Panel b: blue) were stained with DAPI in SlowFade® Gold Antifade Mountant (Product # S36938). F-actin was stained with Rhodamine Phalloidin (Product # R415, 1:300) (Panel c: red). Panel d represents the composite image. No nonspecific staining was observed with the secondary antibody alone (panel f), or with an isotype control (panel e). The images were captured at 60X magnification."

References (of 142 references):
• Nature communications. IFN-β is a macrophage-derived effector cytokine facilitating the resolution of bacterial inflammation. Kumaran Satyanarayanan S,El Kebir D,Soboh S,Butenko S,Sekheri M,Saadi J,Peled N,Assi S,Othman A,Schif-Zuck S,Feuermann Y,Barkan D,Sher.N,Filep JG,Ariel A. 2019.

• Nature communications. The PDGF-BB-SOX7 axis-modulated IL-33 in pericytes and stromal cells promotes metastasis through tumour-associated macrophages. Yang Y,Andersson P,Hosaka K,Zhang Y,Cao R,Iwamoto H,Yang X,Nakamura M,Wang J,Zhuang R,Morikawa H,Xue Y,Braun H,Beyaert R,Samani N,Nakae S,Hams E,Dissing S,Fallon PG,Langer R,Cao Y. 2016.

donkey-anti-mouse-Alexa Fluor 647 (A-31571, 1:1,000)
Validation: "Mouse IgG (H+L) Highly Cross-Adsorbed Secondary Antibody (A-31571) in ICC/IF. Immunofluorescence analysis of Donkey anti-Mouse IgG (H+L) Highly Cross-Adsorbed Secondary Antibody, Alexa Fluor® 647 conjugate was performed using HeLa cells stained with alpha Tubulin (236-10501) Mouse Monoclonal Antibody (Product # A11126). The cells were fixed with 4% paraformaldehyde for 10 minutes, permeabilized with 0.1% Triton™ X-100 for 10 minutes, blocked with 1% BSA for 1 hour and labeled with 2 µg/mL primary antibody for 3 hours at room temperature. Donkey anti-Mouse IgG (H+L) Highly Cross-Adsorbed Secondary Antibody, Alexa Fluor® 647 (Product # A-31571) was used at a concentration of 2 µg/mL in phosphate buffered saline containing 0.2% BSA for 45 minutes at room temperature, for detection of alpha Tubulin in the cytoplasm (Panel a: red). Nuclei (Panel b: blue) were stained with DAPI in SlowFade® Gold Antifade Mountant (Product # S36938). F-actin was stained with Alexa Fluor® 488 Phalloidin (Product # A12379), 1:300) (Panel c: green). Panel d represents the composite image. No nonspecific staining was observed with the secondary antibody alone (panel f), or with an isotype control (panel e). The images were captured at 60X magnification."

References (Out of 142):

• Journal of neurochemistry. The neuroprotective effect of latanoprost acts via klotho-mediated suppression of calpain activation after optic nerve transection. Yamamoto K,Sato K,Yukita M,Yasuda M,Omodaka K,Ryu M,Fujita K,Nishiguchi KM,Machida S,Nakazawa T. 2017

• eLife. Kindlin-2 cooperates with talin to activate integrins and induces cell spreading by directly binding paxillin. Theodosiou M,Widmaier M,Böttcher RT,Rognoni E,Veelders M,Bharadwaj M,Lambacher A,Austen K,Müller DJ,Zent R,Fässler R. 2016.

• Nature cell biology. A human genome-wide screen for regulators of clathrin-coated vesicle formation reveals an unexpected role for the V-ATPase. Kozik P,Hodson NA,Sahlender DA,Simecek N,Soromani C,Wu J,Collinson LM,Robinson MS. 2013.

Eukaryotic cell lines

Policy information about cell lines

Cell line source(s)	HUES8 embryonic cell line from Douglas Melton/Harvard Stem Cell Institute at Harvard University
Authentication	This cell line is a NIH registered human embryonic cell line (NIHhESC-09-0021) that comes from the original source (Douglas Melton) and is available from the Harvard Stem Cell Institute (HSCI). Stem cell cultures were genotyped by STR profile and karyotyped regularly to ensure validity of cell lines used.
Mycoplasma contamination	All cell lines were regularly tested for mycoplasma contamination and tested negative.
Commonly misidentified lines (See ICLAC register)	None

Animals and other organisms

Policy information about studies involving animals; ARRIVE guidelines recommended for reporting animal research

Laboratory animals	Islet donors: C57BL/6 female retired breeders (age not specified/determined as these are random aged retired breeders); Islet recipients: C57BL/6 mice (6-8 weeks old male); Human islet recipients: NOD-scid-Il2rgc-/- (NSG) (Jackson Laboratory, Bar Harbor, ME) mice (age 6-12 weeks, male) Porcine islet recipients: NSG mice (age 6-12 weeks, mixture of male and female)
Wild animals	no wild animals were used in this study.
Field-collected samples	no field-collected samples were used in this study
Ethics oversight	Institutional IACUC committees from the University of Minnesota (protocol #1905-37028A) and the Mayo Clinic (protocol #A00003973) approved the animal studies.

Note that full information on the approval of the study protocol must also be provided in the manuscript.

Flow Cytometry

Plots

Confirm that:

☒ The axis labels state the marker and fluorochrome used (e.g. CD4-FITC).

☒ The axis scales are clearly visible. Include numbers along axes only for bottom left plot of group (a 'group' is an analysis of identical markers).

☒ All plots are contour plots with outliers or pseudocolor plots.

☒ A numerical value for number of cells or percentage (with statistics) is provided.

Methodology

Sample preparation	SC-beta cell clusters were dissociated into single cells, permeabilized, and stained wiht primary and secondary antibodies as fully described in the materials and methods.
Instrument	ThermoFisher Attune flow cytometer
Software	NXT v. 3.1 (ThermoFisher) and FlowJo v.10 (FlowJo, Ashland, OR)
Cell population abundance	Cell sorting was not used in this study
Gating strategy	All captured events are first gated by forward scatter area, side scatter area. Doublet discrimination is performed to define all singlets by gating along the diagonal of forward scatter height, forward scatter width. Final flow cytometry plots for SC-beta characterization are shown as contour plots, with outliers shown. For beta cell specific viability, four-quadrant dot plots are presented with live and dead populations defined from the live/dead marker v. forward scatter area.

☒ Tick this box to confirm that a figure exemplifying the gating strategy is provided in the Supplementary Information.